Amyloids and Micelles

Self-assembly and co-assembly of Abeta and gangliosides

Hu, Jing

2024

Amyloids and Micelles

Self-assembly and co-assembly of Abeta and gangliosides

JING HU | DIVISION OF PHYSICAL CHEMISTRY | LUND UNIVERSITY

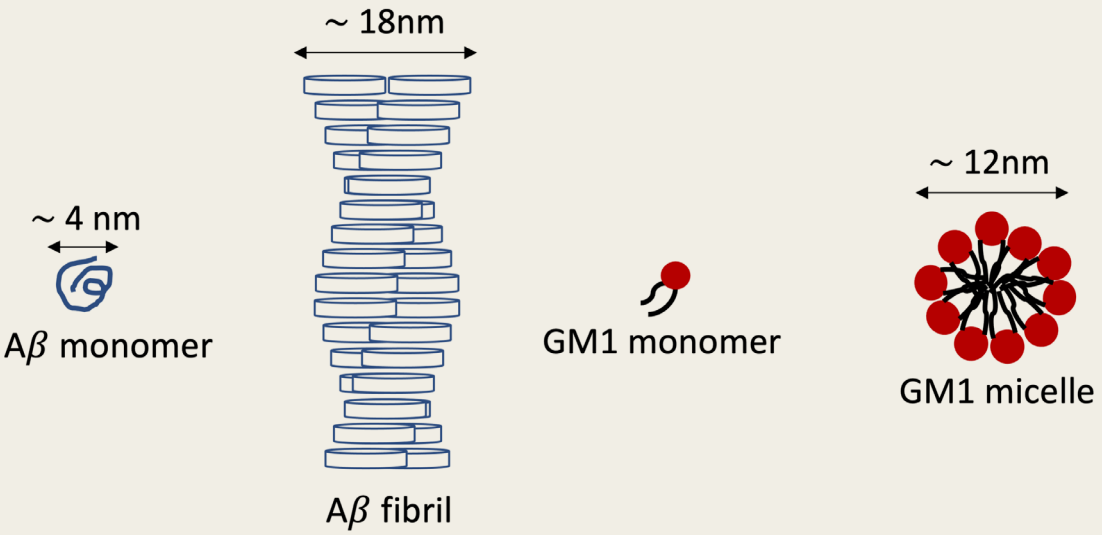

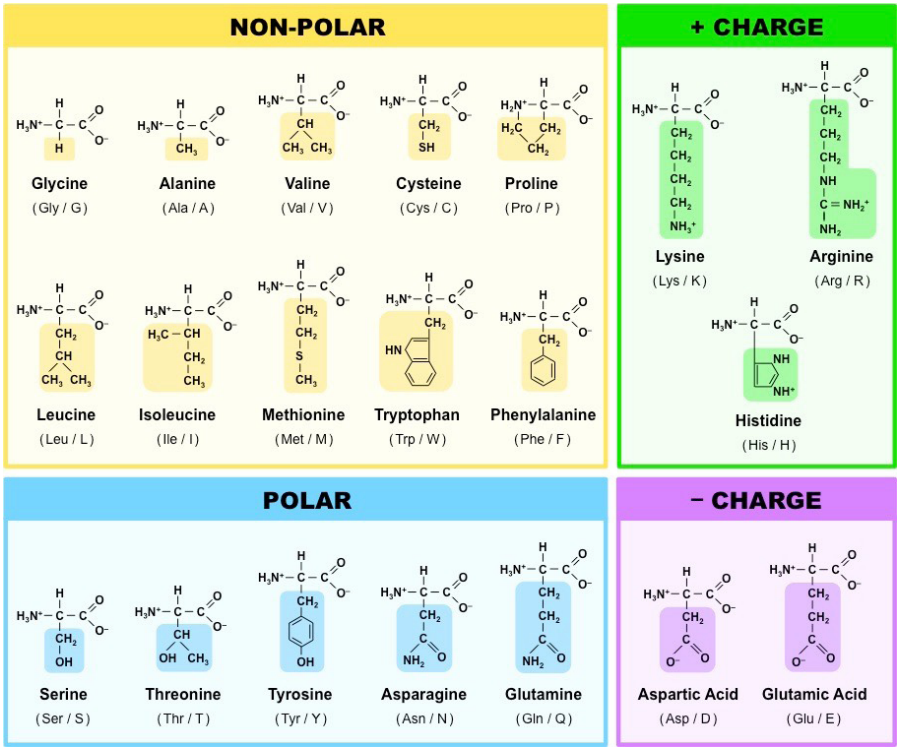

Printed by Media-Tryck, Lund 2025 NORDIC SWAN ECOLABEL 3041 0903

LUND UNIVERSITY

ISBN: 978-91-8096-088-5

Physical Chemistry
Faculty of Science
Lund University

Amyloids and Micelles

Amyloids and Micelles

Self-assembly and co-assembly of Abeta and gangliosides

by Jing Hu

LUND
UNIVERSITY

DOCTORAL DISSERTATION

by due permission of the Faculty of Science, Lund University, Sweden.

To be defended on Friday, the 31st of January 2025 at 9:00 in lecture hall A, Kemicentrum, Lund University.

Faculty opponent

Dr. Christofer Lendel, Division of Applied Physical Chemistry, KTH Royal Institute of Technology, Sweden

Organization
LUND UNIVERSITY

Department of Chemistry
Box 124
SE–221 00 LUND
Sweden

Document name
DOCTORAL DISSERTATION

Date of disputation
2015-12-24

Sponsoring organization

Author(s)
Jing Hu

Title and subtitle
Amyloids and Micelles: Self-assembly and co-assembly of Abeta and gangliosides

Abstract
Extracellular plaques in Alzheimer's disease contain Aβ peptides and ganglioside lipids such as GM1. Aβ monomers self-assemble into beta-sheet-rich fibrils when their concentration exceeds solubility, while GM1 monomers form spherical micelles above their critical concentration. This study examines the self-assembly of Aβ in the first two papers and its co-assembly with GM1 in the last two. In Paper I, we investigate whether the secondary nucleation sites of Aβ are defects on fibrils, using the secondary nucleation sites binding chaperone–Brichos. We found that secondary nucleation sites are rare and that fibrils formed under low supersaturation exhibit fewer secondary nucleation sites than those formed under high supersaturation. In Paper II, we examine the impact of shear force from mild agitation on Aβ kinetics. Our findings show that mild agitation accelerates both primary and secondary nucleation, particularly the detachment step of the latter. Papers III and IV explore the co-assembly of Aβ and GM1 and its effects on Aβ aggregation kinetics and thermodynamics. We found that Aβ and GM1 form micellar co-assemblies, with Aβ evenly distributed among co-assemblies, likely positioned at the interface between GM1's hydrophobic chains and head groups. This co-assembly reduces both the aggregation speed and solubility of Aβ.

Key words
Aβ peptides, ganglioside lipids, kinetic, thermodynamic

Classification system and/or index terms (if any)

Supplementary bibliographical information

Language
English

ISSN and key title

ISBN
978-91-8096-088-5 (print)
978-91-8096-089-2 (pdf)

Recipient's notes

Number of pages
57

Price

Security classification

Amyloids and Micelles

Self-assembly and co-assembly of Abeta and gangliosides

by Jing Hu

LUND
UNIVERSITY

A doctoral thesis at a university in Sweden takes either the form of a single, cohesive research study (monograph) or a summary of research papers (compilation thesis), which the doctoral student has written alone or together with one or several other author(s).

In the latter case the thesis consists of two parts. An introductory text puts the research work into context and summarizes the main points of the papers. Then, the research publications themselves are reproduced, together with a description of the individual contributions of the authors. The research papers may either have been already published or are manuscripts at various stages (in press, submitted, or in draft).

Supervisors:

Professor Emma Sparr

Professor Sara Linse

Cover illustration front: Cartoon adapted from Figure 1 in paper III in the thesis

Cover illustration back: Table of amino acids obtained from https://onlinesciencenotes.com

Faculty of Science, Department of Chemistry

ISBN: 978-91-8096-088-5 (print)
ISBN: 978-91-8096-089-2 (pdf)

Printed in Sweden by Media-Tryck, Lund University, Lund 2025

Contents

List of publications

This thesis is based on the following publications, referred to by their Roman numerals:

I **Secondary nucleation in amyloid formation occurs predominantly at defects in the fibril cross-section.**
Jing Hu, Tom Scheidt*, Dev Thacker*, Thomas Muller, Elin Stemme, Urszula Lapinska, Stefan Wennmalm, Quentin A. E. Peter,Georg Meisl, Samo Curk, Maria Andreasen, Michele Vendruscolo, Paolo Arosio, Andela Saric, Jeremy Schmit, Tuomas P. J. Knowles, Emma Sparr, Sara Linse, Thomas C. T. Michaels, Alexander J. Dear (*contributed equally)
Manuscript

II **The role of shear forces in primary and secondary nucleation of amyloid fibrils.**
Emil Axell*, **Jing Hu***, Max Lindberg*, Alexander J. Dear, Lei Ortigosa-Pascual , Ewa A. Andrzejewska, Greta Šneideriene, Dev Thacker, Tuomas P. J. Knowles, Emma Sparr, Sara Linse (*contributed equally)
Proceedings of the National Academy of Sciences, 121, 25, 2024

III **Ganglioside Micelles Affect Amyloid β Aggregation by Coassembly.**
Jing Hu, Sara Linse, Emma Sparr
ACS Chemical Neuroscience, 14, 24, 2023

IV **Solubilization of Amyloid β by GM1 micelles.**
Jing Hu, Johan Wallerstein, Stefan Wennmalm, Sara Linse, Emma Sparr
Manuscript

Not included in the thesis:

Extracellular Vesicles Slow Down Aβ (1–42) Aggregation by Interfering with the Amyloid Fibril Elongation Step.
Vesa Halipi, Nima Sasanian, Julia Feng, **Jing Hu**, Quentin Lubart, David Bernson, Daniel van Leeuwen, Doryaneh Ahmadpour, Emma Sparr, Elin K Esbjorner
ACS Chemical Neuroscience, 15, 5, 2024

Reduced protein solubility - cause or consequence in amyloid disease?
Max Lindberg, **Jing Hu**, Emma Sparr, Sara Linse
QRB Discovery, accepted

Author Contributions

I I designed the experimental parts of the study together with AJD, SL and ESp. I purified Abeta40 and performed most of the experiments, including the Fluorescence Spectroscopy and Fluorescence Correlation Spectroscopy experiments, Cryo-EM (together with DT) and NMR (together with ESt). I analysed the data with input from co-authors. I wrote the manuscript with AJD and input from co-authors.

II I designed the study together with EA, ML, AD, SL and ES. I preformed the Cryo-EM imaging as well as parts of the amyloid kinetics and Brichos inhibition studies. I contributed to the data analysation and writing of the manuscript with co-authors.

III I designed the study together with the ES and SL. I performed all experiments. I analysed the data with input from co-authors. I wrote the manuscript with input from co-authors.

IV I designed the study together with ES and SL. I performed the NMR experiments together with JW. I performed the other experiments by myself. I analysed the data with input from co-authors. I wrote the manuscript with input from co-authors.

Acknowledgements

I am grateful for the supervision from Emma and Sara. Their support to me is like the support of experienced belayers to a climber. They give me useful, precise and timely suggestions on the routes or positions, if seeing me stuck for too long time, or asking for help. They give me compliments or encouragements for exciting or struggling moments. They are patient, and give me the freedom to explore different routes. Most importantly, I know that they are always there, ready to catch me in case of falling.

I am grateful for the open and collaborative academic environment in the divisions.

I am grateful for the support from all the colleagues, friends, and families.

Popular summary

Proteins are a source of energy, especially for those looking to build muscle. However, some proteins can also lead to diseases, such as prion leads to mad cow disease. Amyloid beta (Aβ) is a protein related to Alzheimer's Disease (AD), but it is yet not known if it is a cause or consequence of AD. Aβ is found in the brain plaques of AD patients. These plaques are abnormal clumps that form between neurons. When the concentration of Aβ exceeds its solubility, it tends to form fibrils, much like how salts precipitate when their solubility is exceeded. The stacking of Aβ monomers in fibrils can be compared to slices of toast stacked on top of one another.

Lipids are also present in the brain plaques, which is not surprising since lipids are essential components of cell membranes. GM1 is a type of lipid found in the same regions as Aβ in these plaques. GM1 has a water-loving headgroup and two water-fearing tails. When GM1 reaches a high enough concentration in water, it self-assembles into spherical structures called micelles, with the headgroups facing water and the tails tucked inside. These micelles look like dandelion seeds. In everyday life, micelles are used in products like soap, where they encapsulate dirt that doesn't dissolve in water.

In Paper I, we explored whether the secondary nucleation sites of Aβ fibrils are defects of the fibrils themselves. Secondary nucleation is a step where existing fibrils act as templates to form new fibrils. This concept is widely used in the crystal industry, where seeds are added to enhance production and ensure consistency of crystals. Our study found that secondary nucleation sites are rare on fibrils, supporting the idea that they may be rare defects. To test this further, we tried "healing" fibrils by increasing the temperature, slowing their formation. The fibrils formed more slowly had fewer secondary nucleation sites and were less efficient at seeding new fibrils.

In Paper II, we examined how mild agitation affects the steps of Aβ fibril formation. We discovered that agitation accelerates primary nucleation (where Aβ monomers come together to form fibrils) and secondary nucleation, but does not affect elongation (where fibrils grow by adding monomers to their ends) or fragmentation (where fibrils break apart). Using electron microscopy, we observed fibrils decorated with transient aggregates, which we interpreted as secondary nucleated fibrils. Agitation appears to shear these newly formed fibrils away from their template fibrils, speeding up their detachment.

In Papers III and IV, we studied how GM1 micelles interact with Aβ. Like soap dissolving dirt, GM1 micelles solubilize Aβ. The water-fearing parts of Aβ

embed themselves in the oily core of the micelles, while the water-loving parts want to remain exposed to water. We found that the addition of GM1 micelles delays the formation of Aβ fibrils and increases the apparent solubility of Aβ. This "apparent solubility" includes both Aβ dissolved in water and Aβ dissolved in micelles.

The findings presented in this thesis can have implications to the understading of AD.

Introduction

1 Aβ and GM1

The cleavage of amyloid precursor protein (APP), a transmembrane protein expressed in neurons, produces Aβ peptides with varying lengths, of which the 40 and 42 amino acids peptide – Aβ40 and Aβ42 - are most abundant [1]. Aβ40 and Aβ42 are peptides naturally produced in cells of all human individuals throughout our lives. The concentration of Aβ40 and Aβ42 in both tissues and the brain have been shown to be lower in cognitively normal elderly individuals than in patients with AD [2, 3]. While the concentration of Aβ42 in CSF is higher in healthy controls than in patients with AD [4, 5]. Amyloid plaques– extracellular deposits that are primarily composed of fibrillar Aβ deposits–are a neuropathological hallmark of Alzheimer's Disease (AD), motivated by the fact that these plaques are consistently observed in the brains from individuals with AD [6, 7]. It is therefore essential to understand the molecular mechanism of Aβ self-assembly into fibrils. This can be done by studying its kinetic steps and thermodynamic driving forces for peptide aggregation, and by identifying factors that influence this aggregation process.

The AD amyloid plaques also include non-amyloid lipid-rich constituents, such as extracellular vesicles, extracellular multilamellar bodies, and cellular compartments [7]. Monosialotetrahexosylganglioside (GM1) is one of the major ganglioside lipids found to be enriched and colocalized with Aβ40 in the core region of mature plaques [8]. GM1 is present at relatively high concentrations in the brain, with an approximate concentration of 8 pmol/mg (equivalent to 8 μM, assuming a tissue density of 1 g/mL) [9]. It is also found that the GM1 concentration changes during aging and across different neuropathological conditions [10].

With this background, the following questions are addressed in this thesis: What factors affect the different steps of the Aβ aggregation reaction? In the first

part of the thesis, we investigate how external factors like mild agitation (shear forces) and temperature affect the reaction. We also study in detail how defects on the fibril surface may promote the aggregation process. In the second part of the thesis, we investigate the interactions between Aβ and GM1 gangliosides, to elucidate the effects of gangliosides on the equilibrium and the kinetic steps of Aβ aggregation.

2 The self-assembly of GM1 to form micelles

2.1 Why do GM1 monomers form micelles?

GM1 is an amphiphilic molecule that possesses a polar head group and nonpolar hydrocarbon chains, as shown in Fig. 1 (a). The head group of GM1 contains four sugar residues and one sialic acid with a pKa of ca. 2.7 [11], thus GM1 is negatively charged at the pH values used in this thesis. To minimize the unfavorable interactions between the hydrophobic GM1 hydrocarbon chains and water, GM1 self-assembles to create a microphase in which the hydrophobic chains sequester themselves inside the aggregate and the polar head groups orient themselves toward the aqueous phase [12]. However, electrostatic and entropic steric repulsion between the head groups opposes the increase of the aggregate size, leading to a finite size of the aggregate, which is a characteristic of micelles. Adding more GM1 results in the formation of more micelles of similar size. A useful guide for predicting the aggregate structure in dilute solutions is the surfactant parameter $N_s = \frac{v}{la_0}$, where v, l, and a_0 represent the volume of the hydrophobic part of the amphiphile, the length of the hydrocarbon chains, and the effective area per head group, respectively [12]. The effective area per head group reflects the opposing tendencies of the head group to crowd close together, i.e., electrostatic repulsion, entropic steric repulsion, steric hindrance, and hydration. As shown in Fig. 1(b), amphiphilic molecules with $N_s \leq 0.33$ have a packing shape of a cone and favor the formation of spherical micelles. GM1 is one of the amphiphilic lipids that forms spherical micelles due to its large sugar-based, negatively charged head group. Other examples of micelle-forming lipids are lysolipids and fatty acids [13].

2.2 Characterization of GM1 micelles

The critical micelle concentration (CMC) is defined as the concentration at which amphiphiles reach their maximum solubility. At higher concentrations,

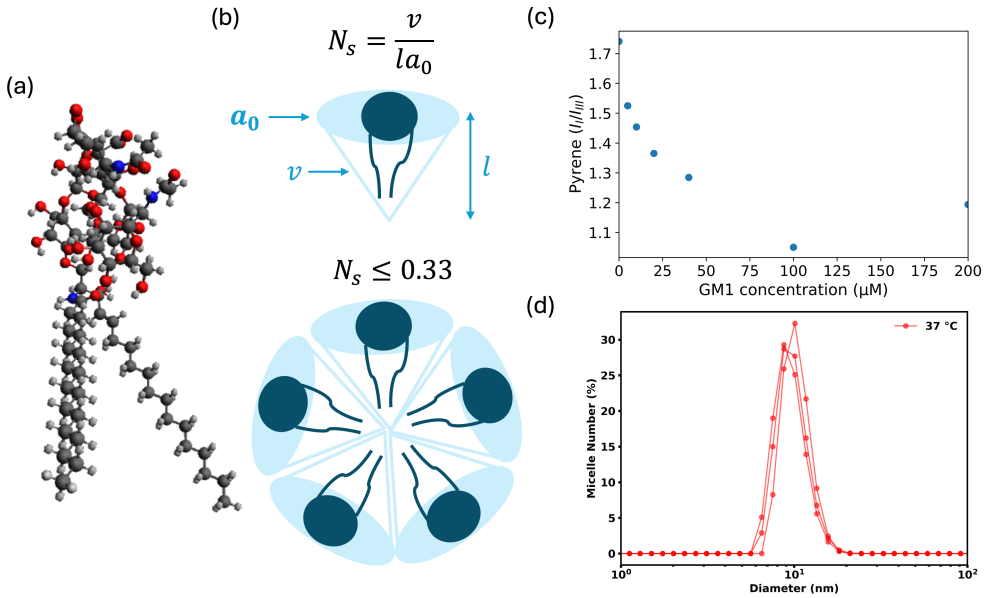

Figure 1: **a**: 3D chemical structure of GM1, with red, blue, dark grey, grey spheres representing oxygen, nitrogen, carbon and hydrogen, respectively. **b**: Light blue cartoon shows the parameters in surfactant number, with light blue representing the critical packing shape of cone. Dark blue cartoon represents GM1 with a headgroup and two tails. **c**: The ratio of the first (around 373 nm) and third (around 384 nm) peak is from the fluorescence spectra of samples containing pyrene and different concentration of GM1. **d**: GM1 micelle size distribution based on the dynamic light scattering of 80μM GM1 at 37°C.

micelles begin to form. As the concentration of the amphiphile increases, the number of micelles grows, while their size remains virtually unchanged over a wide range of concentrations [12]. The CMC of GM1 was here measured by pyrene fluorescence spectroscopy assay to be less than 5 μM (paper III). As shown in Fig. 1(c), already the addition of 5 μM GM1 has an effect on the pyrene spectrum, here illustrated by the ratio between the intensity of the first and third peaks in the spectrum. This indicates that the sample contains micelles already at this low concentration. The concentration of GM1 used for all experiments in this thesis is above 5 μM, as we are interested in the interaction between GM1 micelles and Aβ. We also measured the size distribution of GM1 micelles based on dynamic light scattering on samples containing 80 μM GM1. Fig. 1(d) shows that the diameter of GM1 micelles ranges from 7 to 11 nm, with most objects having a diameter of around 10 nm. This is consistent with GM1 size measured by microfluidic diffusional sizing and cryo-TEM (Paper III), as well as with previous studies in the literature [14]. From previous mass spectrometry analysis [15], we know that most GM1 molecules contain 18 or 20 carbons, and the fully extended acyl chains thus have a length of ca. 2.5 nm ($l = 0.15 + 0.12 \cdot n_c$, where n_c = 18–20) [12]. The GM1 headgroup is five residue branch oligosaccharides.

Given the length of a glucose molecule, approx. 0.8 nm in the long axis [16], the length of the extended GM1 oligosaccharide headgroup can be estimated at roughly 2.5-3.0 nm. This gives rise to a total estimated length of the fully stretched GM1 lipid molecule of around 5.0-5.5 nm. The diameter of the micelle is expected to be roughly twice the length of the molecule, that is, around 10-11 nm. This estimation is consistent with the observed size of GM1 micelles in Fig. 1(d) and the measured hydrodynamic radius in paper III.

The aggregation number of GM1 can be estimated for a sphere with given volume (eg diameter of 10 nm in line with cryo-TEM data of GM1 in paper III) , assuming that the density of GM1 micelles is close to the density of water, and knowing the molecular weight of GM1 (1569 g/mol). This gives an estimate of GM1 micelle aggregation number of ca 200, which aligns with reported values [17]. The rate at which amphiphilic molecules come together to form micelles is largely diffusion limited, as the monomer association reaction involves no slow structural reorganization or bond formation. For example, the rate of some sodium alkyl sulfate micelle formation and disintegration is in the ms range [12], and the rate of monomer exchange between micelles is in the μs range. It is good to note that these timescales are also affected by the monomer solubility in the limit where it is low. For example, self-assembly rate of ionic single-chain surfactant is generally diffusion limited, but for more hydrophobic molecules the solubility will also play a role.

2.3 Models describing micelle formation

The first step for micelle formation is similar to that of phase separation: above a certain concentration, the monomers spontaneously self-assemble to form a separate structure with different physical properties compared to those of free monomers in the solvent. Now consider a system of one type of amphiphilic molecule in water (or another solvent). At equilibrium, the chemical potential of the amphiphilic molecule in the micelle ($\mu_{i,\text{micelle}}$=$\mu^{\Theta}_{i,\text{micelle}}$) is equal to the chemical potential of the monomer in the (dilute) solution ($\mu_{i,\text{solution}} = \mu^{\Theta}_{i,\text{solution}} + RT\ln[X_i]$), where R is the gas constant, T is temperature, and $[X_i]$ is the mole fraction of molecule i. The phase separation model [12] approximates micelle formation as a phase separation process that occurs at a well-defined critical concentration (CMC). At equilibrium, $\mu^{\Theta}_{i,\text{micelle}} = \mu^{\Theta}_{i,\text{solvent}} + RT\ln\text{CMC}$.

However, the phase separation model does not account for the stop mechanism of micelle formation; that is, micelles have a finite and well-defined aggregation number, meaning that when more amphiphiles is added, one gets more micelles of the same size rather than larger aggregates. This stop mechanism

can be described by the closed-association model, assuming that only monomers and micelles with aggregation number N exist in the system at concentrations above the CMC. The closed-association model will lead to the same equation as the phase separation model under the approximation of infinite N, with the combination of $\Delta G^{\Theta} = -RT \ln K$, where K is the equilibrium constant for N monomers forming one aggregate.

3 Self-assembly of Aβ to form fibrils

3.1 Kinetics of fibril formation

Above a certain concentration, Aβ40 or Aβ42 aggregate into amyloid fibrils. The kinetics of amyloid formation can be monitored using fibril-sensitive dyes, such as ThT and pFTAA. These dyes typically emit fluorescence with higher intensity in the presence of fibrils compared to monomers, and the fluorescence intensity is positively correlated to fibril mass [18]. Such experimental data can then be fitted by kinetic models in order to reveal the importance and rate constants of the different steps of the aggregation reaction [19, 20].

The microscopic steps of the kinetic models used in amyloid aggregation online fitting tool–amylofit are: primary nucleation, elongation, secondary nucleation and fragmentation. [19, 20] Primary nucleation is the step during which protein monomers come together in solution to form a small, energetically stable structure. Elongation is the step during which monomers bind to the growing fibril ends, leading to fibril growth. Secondary nucleation is the step during which existing fibrils catalyze the formation of new aggregates by interacting with free monomers. Fragmentation is the step during which fibrils break into smaller pieces, which can be caused by mechanical forces, thermal fluctuations, or chemical interactions. For Aβ40 or Aβ42 under non-shaking conditions at pH 7.4, 37°C, the kinetic model involves an initial primary nucleation step followed by fibril elongation and secondary nucleation (Fig. 2(b)). Fragmentation is negligible for Aβ40 and Aβ42 under normal conditions but can play an important role in other instances, such as under vigorous shaking [21].

In the kinetic model described above [20], the Aβ40 or Aβ42 increase in fibril mass concentration can be described by the following equation:

$$\frac{d[M]}{dt} = 2k_{+}[m][P] \tag{1}$$

where the mass concentration of the fibrils $[M]$ is related to the elongation rate constant k_+, the mass of monomers $[m]$ at time t, and the number concentration of fibrils $[P]$ at time t, as elongation influences only the mass and not the number of fibrils. The fibril number concentration is related to both primary and secondary nucleation, contributing to fibril increase through the following equation:

$$\frac{d[P]}{dt} = k_n[m]^{n_c} + k_2 \frac{[m]^{n_2}}{1 + \frac{[m]^{n_2}}{K_M}}[M] \tag{2}$$

where k_n, k_2, and K_M are the primary nucleation rate constant, secondary nucleation rate constant, and secondary nucleation saturation constant, respectively. n_c and n_2 are the reaction orders of primary and secondary nucleation.

Integration of equation (1) and equation (2) leads to an equation that describes the normalized fibril mass concentration $\frac{M(t)}{M_\infty}$ over time t [20]:

$$\frac{M(t)}{M_\infty} = 1 - \left(1 - \frac{M_0}{M_\infty}\right) e^{-k_\infty t} \left(\frac{B_- + C_+ e^{\kappa t}}{B_+ + C_+ e^{\kappa t}} \frac{B_+ + C_+}{B_- + C_+}\right)^{k_\infty/\kappa} \tag{3}$$

where

$$\kappa = \sqrt{2[m]_0 k_+ \frac{[m]_0^{n_2} k_2}{1 + \frac{[m]_0^{n_2}}{K_M}}}$$

$$\lambda = \sqrt{2k_+ k_n [m]_0^{n_c}}$$

$$C_\pm = \frac{k_+[P]_0}{\kappa} \pm \frac{k_+[M]_0}{2[m]_0 k_+} \pm \frac{\lambda^2}{2\kappa^2}$$

$$k_\infty = 2k_+[P]_\infty$$

$$\bar{k}_\infty = \sqrt{k_\infty^2 - 2C_+C_-\kappa^2}$$

$$B_\pm = \frac{k_\infty \pm \bar{k}_\infty}{2\kappa}$$

Equation(3) can be fitted to experimental kinetic traces. From the global fitting to a set of experimental data obtained at different conditions, one can obtain

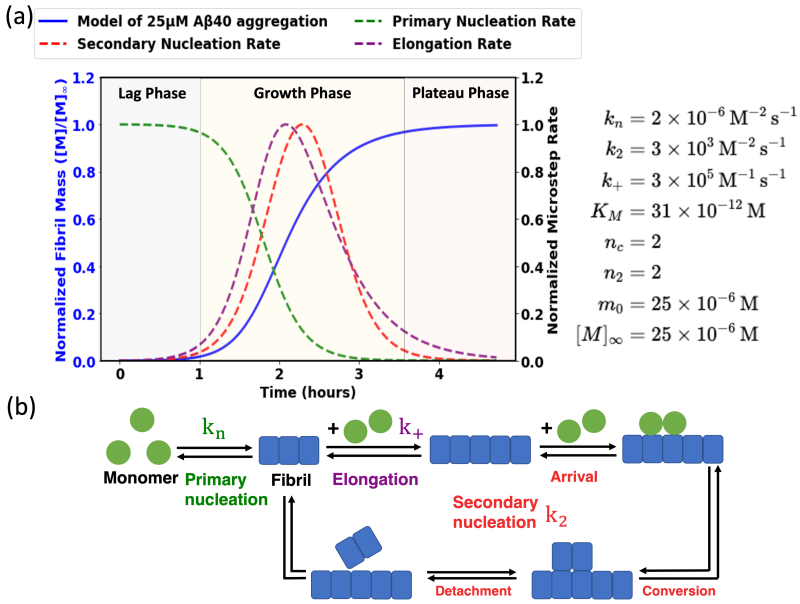

Figure 2: **a**:Normalized mass of Aβ40 fibrils calculated from equation(3) with m_0 of 25 μM. The input parameters on the right of the plot are gained from a previous published paper[20]. The infinite mass concentration of fibril is chosen to be 25 μM. The rate of primary, secondary and elongation is also plotted against time, and normalized by the maximum rate of each. **b**: The cartoon shows the relationship between the microscopic steps that play a role in the aggregation of Aβ40 or Aβ42 in condition of pH 7.4, 37 degrees, non-shaking.

values of the different rate constants and reaction orders: k_n, k_2, K_M, n_c, n_2. Other parameters like initial monomer concentration $[m]_0$, initial fibril mass and number concentration, $[M]_0$ and $[P]_0$, final fibril mass concentration, $[M]_\infty$ can be fixed according to experimental conditions, while final fibril number concentration $[P]_\infty$ can be converted from $[M]_\infty$ assuming an average fibril length of 1.3 μm (28000 monomers per fibril)[20]. To illustrate how the different rate constants affect the aggregation process, Fig. 2(a) shows a calculated kinetic trace for an example sample that contains 25 μM Aβ40 monomers. The model takes into account elongation and secondary nucleation but not fragmentation. The input parameters used for these example calculation are chosen as being typical values for Aβ40 under conditions of pH 7.4, 37°C, non-shaking[20].

One can also calculate the rates of primary nucleation, secondary nucleation, and elongation given by: $\frac{d[P]}{dt} = k_n[m]^{n_c}$, $\frac{d[P]}{dt} = k_2 \frac{[m]^{n_2}}{1+\frac{[m]^{n_2}}{K_M}}[M]$, and $\frac{d[M]}{dt} = 2k_+[m][P]$, respectively. The rate of each microscopic step is normalized to its maximum value, removing units and allowing for an easy comparison of how the rate of each step changes over time. As shown in Fig. 2(a), the primary nucleation rate decreases over time due to the declining monomer concentration.

In contrast, both secondary nucleation and elongation rates peak around the halt-time of aggregation, as they depend on the presence of both monomers and fibrils. Similar finding has been presented for Aβ42 at pH 8.0 [22].

3.2 Thermodynamics of fibril formation

In conditions where the system containing Aβ monomers and fibrils reaches equilibrium, the chemical potential of monomers in fibrils is equal to the chemical potential of monomers in the solution, $\mu_{i,\text{fibril}} = \mu_{i,\text{solution}}$. Fibril formation can be described in terms of a solution-solid phase seperation, as the concentration of monomers in solution remains constant above a certain concentration that is the protein solubility [23]. Thus, there is a thermodynamic drive for fibril formation that occurs at all concentrations above the solubility concentration, denoted by S. At equilibrium, the chemical potential of peptide in solution $\mu_{i,\text{solution}} = \mu^{\ominus}_{i,\text{solution}} + RT \ln S = \mu^{\ominus}_{i,\text{fibril}}$. The last equality follows from that the fibrils are considered as the pure solid state, which is also the standard state.

In practice, reaching equilibrium in the amyloid system is often a very slow process. In samples where the initial monomer concentration is very close to S, the system can, in some cases, become trapped in a metastable state for several days due to high nucleation barriers preventing fibril formation [24]. In fact, it is commonly observed that fibrils of different morphologies co-exist in the amyloid system[25, 26], while only the most stable structure can be the equilibrium structure. Equilibrium can be verified by approaching it from multiple directions [27], as demonstrated in Paper IV by monitoring both the aggregation of monomers and the dissociation of fibrils.

Methods

In this methods section, I introduce several key techniques that are repeatedly used throughout this thesis. These include confocal microscopy as well as quantitative methods that are combined with the confocal microscope, such as Microfluidic diffusional sizing (MDS) and Fluorescence Correlation Spectroscopy (FCS). The latter methods play a crucial role in characterizing molecular diffusion in dilute solutions. Specifically, they were employed to study the diffusion of Aβ monomers (Papers III and IV), Aβ oligomers (Paper II), Aβ-GM1 micellar co-assemblies (Papers III and IV), and chaperones that binds to the Aβ secondary nucleation sites (Paper I). Additionally, cryo-EM is introduced as a method for imaging Aβ fibril morphology, as utilized in Papers I, II, and III. Lastly, NMR spectroscopy is heavily used in Paper IV. Below, these key methods are introduced focusing on how they are used in the present studies.

4 Fluorescence Laser Scanning Confocal Microscopy

In a wide-field fluorescence microscope, both in-focus light (red lines in Fig. 3(a)) and out-of-focus light from other focal planes (red dotted lines in Fig. 3(a)) or diffraction and scattering from other points outside of the focus point can reach the detector. To generate a focus spot of illumination, the confocal microscope system is equipped with the detecting pinhole, which prevents the out-of-focus light from reaching the detector, as shown in Fig. 3(a). In addition, the illuminated pinhole facilitates the formation of a point light source with strong directivity, small divergence, and high brightness [28]. However, since the microscope with pinholes only provides information about a single point at a time, the focused spot of light must be scanned across the sample to build an image [29]. The advantage of fluorescence laser scanning confocal microscopy is thus high resolution and optical sectioning [30]. In the present thesis, confocal microscopy was used in Paper III.

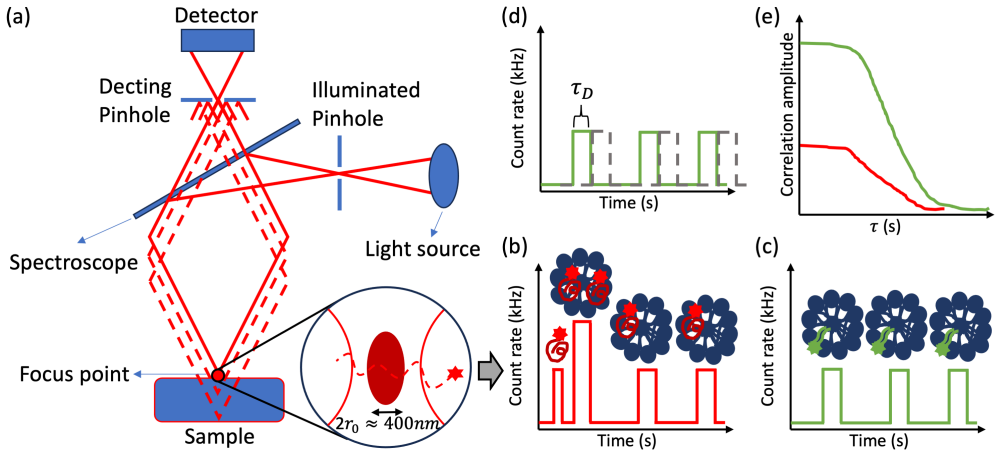

Figure 3: **a**: Graphical depiction of fluorescence laser scanning confocal microscopy. The zoom in of the focus point shows the fluorescence correlation spectroscopy detection volume with a fluorescent molecule passing through. **b** and **c**: Schematic count rate-time plot for sample containing Alexa647-Aβ42 monomers inside or outside micellar aggregates, and GM1 micelles with Oregon Green 488 DHPE, respectively. **d**: Schematic plot of figure **c** (green) and figure **c** shifted by τ_D to the right (grey). **e**: Schematic autocorrelation curves for data in fiogure **b** and **c**.

5 Fluorescence Correlation Spectroscopy (FCS)

FCS employs a confocal microscopy setup to create a small observation volume at the focal point [31]. In Fig. 3(a), the confocal detection volume is represented by the red oval, with r_0 representing the lateral radial distance of the detection volume, which is around 200-300 nm in our FCS experiments. This small detection volume allows for the measurement of individual molecules as they diffuse through the focal volume. Theoretically, as a fluorescently labeled object enters and exits the observation volume, it generates a spike in the count rate-time plot [32, 33]. The count rate reflects the number of counted photons per unit time, corresponding to the fluorescence intensity. The duration of a molecule within the detection volume determines the spike width, while the number of fluorescent dyes carried by the molecule affects the spike height.

In paper III and IV, samples composed of Alexa647-Aβ42 and GM1 were investigated. The Alexa probe can either be present in peptide monomers in solution or in peptides associated with GM1 micelles. If the micellar aggregates are bigger than Alexa647-Aβ42 monomers, the spike from the Alexa647-Aβ42 in micellar aggregates will be broader than free Alexa647-Aβ42 monomer (Fig. 3 (b) and (c)). The spikes for GM1 micells doped with Oregon Green 488 DHPE are of similar width due to the uniform size of micelles. The height of the spike corresponding to two Alexa647-Aβ42 in the co-assembly will be higher than that of one Alexa647-Aβ42 in the co-assembly or Alexa647-Aβ42 monomers. In real

measurements, the number and the shape of the spikes vary more than in the ideal example described above. To analyze the data, we extracted the autocorrelation functions (Equation 4) of the intensity time traces to extract the particle diffusion time and particle number [34, 35].

$$G(\tau) = \frac{\langle \delta I(t) \cdot \delta I(t+\tau) \rangle}{\langle I \rangle^2} \tag{4}$$

Here, $\langle I \rangle$ is the time-averaged intensity, and $\delta I(t)$ is the zero-mean fluctuations on top of $\langle I \rangle$, that is $\delta I(t) = I(t) - \langle I \rangle$. To understand the meaning of the autocorrelation function in these experiments, we can imagine that the intensity-time trace is shifted with a distance of τ in the plot (gray dotted lines in Fig. 3 (d)). The correlation amplitude in Fig. 3 (e) represents the correlation between the original and shifted intensity-time trace. The autocorrelation function decays as τ increases, indicating that fluctuations in intensity become uncorrelated over time, and drops to minimum when τ=τ_D, where τ_D is the average retention time of particles in the focal volume. The green and red curves in Fig. 3 (e) represents the autocorrelation funtion obtained from ig. 3 (c) and (b), respectively. The red curve decays faster compared to the green curve, corresponding to shorter average diffusion time of Alexa647-Aβ42 (within a micellar aggregate or present as free monomer in solution) compared to that of GM1 micelles with Oregon Green 488 DHPE.

The autocorrelation curve can be fitted using models with different particle size distribution. For example, a simple single-species model [36]: $G(\tau) = \frac{1}{N}\left(\frac{1}{\left(1+\frac{\tau}{\tau_D}\right)\sqrt{1+\frac{\tau}{\tau_D S^2}}}\right) + 1$, N is the particle number, and S is the structure parameter, which is fixed at the same value for all fits since it is related to the detection volume. The population-averaged τ_{D} obtained from the fitting can be used to estimate the population-averaged diffusion coefficient of the labeled species as [37]: $\tau_D = \frac{r_0^2}{4D}$. The zero-lag amplitude of $G(\tau)$ is inversely proportional to the average number of particles N in the detection volume. In addition to average particle number, FCS can also provide the particle number distribution, plotted as a histogram of spike count rate in Fig. 3 (b) and (c) [38]. For example, in paper IV, we detected the number distribution of Alexa647-Aβ42 in micellar aggregates at different Aβ/GM1 ratios.

6 Microfluidic diffusional sizing (MDS)

Just as for FCS, the single-molecule MDS employs a confocal microscopy setup to scan the sample, but in the case of MDS one scan different positions in a microfluidic channel [39]. The working principle of MDS with sample containing free Alexa647-Aβ42 and Alexa647-Aβ42-GM1 micellar aggregates is shown in Fig. 4(a), where the sample is slowly injected (typically around 100 μL/h) with pure buffer on two sides into a microfluidic channel. The goal of slow injection is to create a smooth, layered flow of liquid, known as lamellar flow. This smooth flow prevents molecules from randomly swirling around. Because of this orderly movement, the only way particles spread out in the Y-Z plane over time (as X increases) is through diffusion from areas of higher concentration (channel center shown as a dotted grey line) to areas of lower concentration (channel edge). The diffusion coefficient (or diffusion time) depends on the size of the diffusing object. Here, the radius of free Alexa647-Aβ42 is smaller than that of micelles, thus free Alexa647-Aβ42 diffuses further towards the channel edge compared to micelles. It is worth mentioning that the radius of GM1 micelles is almost 100 times less than the radius of the focal volume, r_0, thus the cartoon of micellar aggregates in the schematic is not representing their real size.

The confocal detection volume is moved at a constant speed across the Y direction at the mid-height of the microfluidic channel, and also moved to several different X positions. The schematic photon count detected by the confocal microscope versus the channel position at four different X positions is plotted in Fig. 4(b). As the X values increase, the peak widens, showing that fluorescent particles spread more from the center of the channel toward the edges over time. By comparing the observed diffusion profiles with simulated profiles of spherical particles undergoing both advection and diffusion in microfluidic channels [40], we can determine the distribution of hydrodynamic radius for the labeled molecules.

7 Cryogenic Electron Microscopy (Cryo-TEM)

The image resolution of light microscopy, as defined by the classic Rayleigh criterion [41], states that the smallest resolution (δ) is given by:

$$\delta = \frac{0.61\lambda}{\mu \sin \beta} \tag{5}$$

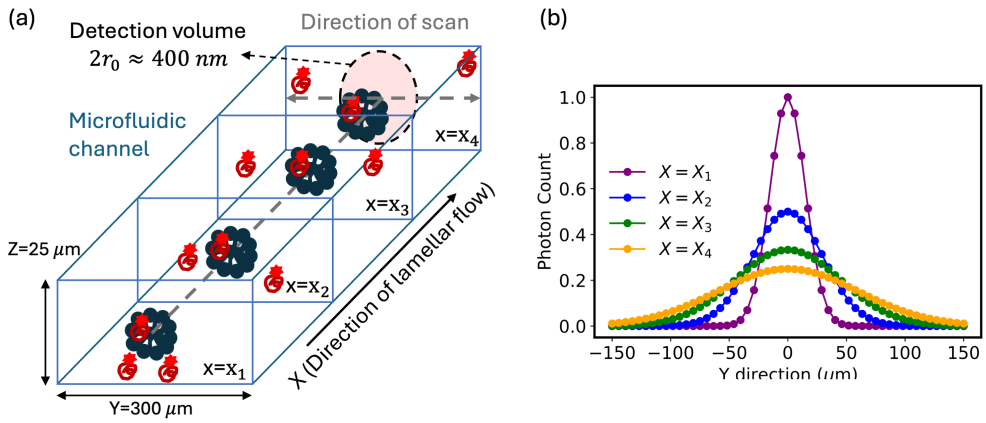

Figure 4: **a**: Graphical depiction of working principle of MDS with sample containing free Alexa647-Aβ42 and Alexa647-Aβ42-GM1 micellar aggregates. **b**: Schematic diffusion profiles of molecules through the channel cross-section recorded at different x locations along the microfluidic channel.

In Equation 5, λ is the wavelength of the light, μ is the refractive index of the viewing medium, and β is the semi-angle of collection of the magnifying lens. The numerical aperture ($NA = \mu \sin \beta$) of a microscope objective typically ranges from about 0.1 to 1.4. Therefore, with visible light wavelengths around 400–700 nm, the best achievable resolution is roughly 200 nm [42]. This limitation has been overcome in super-resolution fluorescence microscopy, yet the image resolution of light microscopy has not surpassed 10 nm. In contrast, electron microscopy achieves higher resolution due to the much shorter wavelength of electrons.

In Transmission Electron Microscopy (TEM), "transmission" refers to the use of transmitted electrons, which pass through the sample to form an image. This is different from Scanning Electron Microscopy (SEM), where electrons are reflected off the surface, providing surface-level information. TEM, by contrast, enables visualization of internal structures since it "sees through" the sample, which in the present studies contains fibrils or micelles in buffer solution (paper I and III). In order for TEM to work, the specimen must be thin enough to transmit sufficient electrons, ensuring adequate intensity on the detector.

To achieve a sufficiently thin layer of liquid sample, one can apply the sample to a grid coated with a holey carbon support film and then blot the grid nearly dry by pressing a piece of filter paper on the grid. Next, we vitrify this thin layer of sample on the grid by plunging it into a bath of cryogen liquid (ethane in our case) maintained near its freezing point (-169 °C). This temperature is stabilized by a reservoir of liquid nitrogen. Vitrification, rather than crystallization (i.e.,

ice formation), occurs because of the rapid cooling well below water's freezing point and the thinness of the sample layer (around 0.2 mm or less) [43]. Vitrification allows proteins and micelles to retain their native hydrated structure at atomic resolution, while making the samples suitable for the vacuum conditions of TEM [44].

8 Nuclear Magnetic Resonance (NMR) spectroscopy

NMR spectroscopy provides information on the local electronic structure around atomic nuclei [45]. A brief introduction to the basics of NMR spectroscopy's working principle is given in reference [46]. In an NMR experiment, for example the one described in paper IV, an external magnetic field (B_0) creates a magnetization in the sample due to the intrinsic nuclear spin and the the magnetic moments interlinked with the spin. The magnetization is parallel to the external B_0-field, has a frequency $\omega_0{=}\gamma B_0$, where γ is the gyromagnetic ratio with units rad s^{-1} T^{-1} and equals 267522205 rad s^{-1} T^{-1} for protons, for the magnetic field 18.8 T used in paper IV, this results in a proton Larmor frequency of 800 MHz. On the magnetized sample, another magnetic field (B_1) is applied perpendicular to B_0 using a radio frequency pulse with a much weaker field strength than B_0. The radio frequency of B_1 electromagnetic pulse is in resonance with the nuclei of interest (^{1}H or ^{15}N in this thesis). Thus, B1 can rotate the net nuclear magnetizations of the nuclei to a certain angle, depending on the duration and strength of the pulse. The signal is detected by the receiver coil during the relaxation of nuclei back to the original longitudinal state, and it is referred to as the free induction decay (FID). A Fourier transformation of the FID converts the time domain to the frequency domain and we get an NMR spectrum. The detected frequencies are normalized by the spectrometer frequency, resulting in the B_0-field independent chemical shift scale with units of ppm.

As is shown in figure Fig. 5(a), the ^{1}H nuclei in the GM1 lipid tails give rise to peaks resonance in the low ppm region, while ^{1}H in the head group and glycosidic linkage resonances at higher ppm values due to differences in their electronic environments. The hydrogens in the lipid tails are part of the aliphatic (nonpolar) chains, with strong electron shielding. In contrast, the head group and glycosidic linkage regions contain more electronegative atoms, such as oxygen and nitrogen, which withdraw electron density from nearby hydrogen atoms. This electron withdrawal reduces shielding, causing these hydrogens to resonate at higher ppm.

By introducing a 2nd indirect dimension into the pulse sequence we can ac-

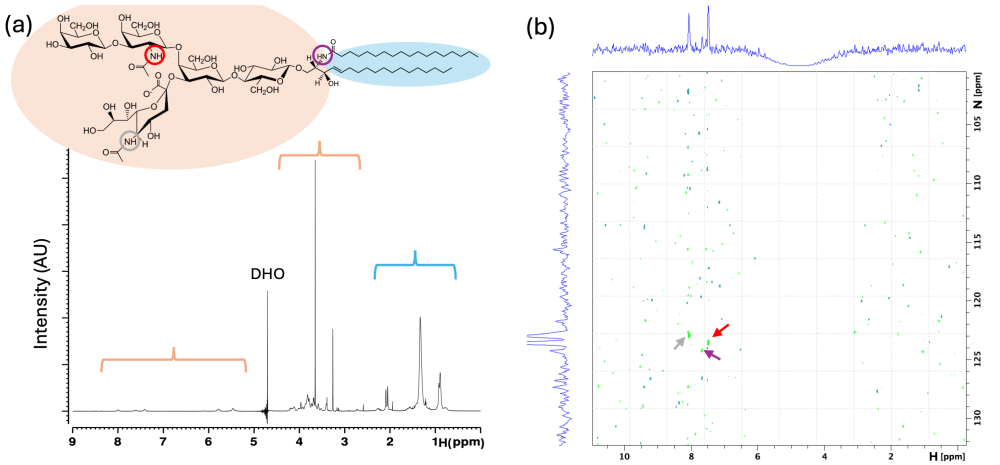

Figure 5: **a**: 1D ^{1}H NMR spectrum of 889 μM GM1 with the chemical structure of GM1 on top. **b**: 2D ^{1}H ^{15}N HMQC spectrum of 2 mM GM1, with the arrows pointing at the peaks of GM1. The positive peaks are light green, while negative peaks are dark green. The projections of the spectrum at both x and y axis are plotted on the top and left side of the spectrum.

quire correlations between ^{1}H and ^{15}N nuclei and we get a 2D NMR spectrum (Fig. 5(b). In a 2D ^{1}H ^{15}N Heteronuclear Multiple Quantum Coherence (HMQC) spectrum, the x-axis represents the ^{1}H chemical shifts, while the y-axis represents the ^{15}N chemical shifts. Each cross-peak in the 2D spectrum represents a specific ^{1}H-^{15}N pair, where hydrogens are directly bonded to nitrogens. For example, the NH groups in GM1 are shown as three cross-peaks pointed by the arrows, while the ^{1}H connected to carbon or oxygen are filtered out from the spectrum. This ^{1}H ^{15}N spectra is especially valuable for studying proteins since every amino acid except proline has an amide group with a nitrogen-bound hydrogen, resulting in unique cross-peaks in the 2D spectrum that create a "fingerprint" for the protein.

Aβ aggregation and the effects of GM1

9 Secondary nucleation – arrival and detachment

9.1 Introduction to secondary nucleation

Secondary nucleation in amyloid formation corresponds to the reaction step in which protein aggregation is nucleated in the presence of fibrils, which will then lead to the formation of new fibrils. The secondary nucleation process may occur on the side surface of fibrils. Secondary nucleation is considered to be of critical importantance in amyloid formation as this aggregation reaction step has been found to be crucial to the aggregation of many disease-related amyloid-forming proteins [47, 48, 49]. For many systems of aggregating proteins [50, 51, 52], the secondary nuclation is also responsible for oligomer production under standard *in vitro* reaction conditions (i.e. pH 7.4). Rapid secondary nucleation is characteristic of disease-associated amyloids, due to both its autocatalytic effect on fibril proliferation and its ability to produce large quantities of oligomers [53]. Its inherently catalytic nature leads to enzyme-like kinetics, with the reaction rate saturating at high enough monomer concentrations [20, 54]. As shown in the doubly logarithmic plot (Fig. 6(a)), for kinetics dominated by secondary nucleation at low initial monomer concentration, the slope is equal to $(n_2+1)/2$ and typically around -1.4 [55], with n_2 being the monomer reaction order of secondary nucleation step. At high initial monomer concentration, the secondary nucleation sites on the fibril surfaces become fully occupied by monomeric protein, resulting in a loss of dependence of the secondary nucleation rate on monomer concentration. Analogous to Michaelis–Menten enzyme kinetics [56], secondary nucleation is modeled as a multistep process in the kinetic models commonly used to describe amyloid formation [19]. These steps include asso-

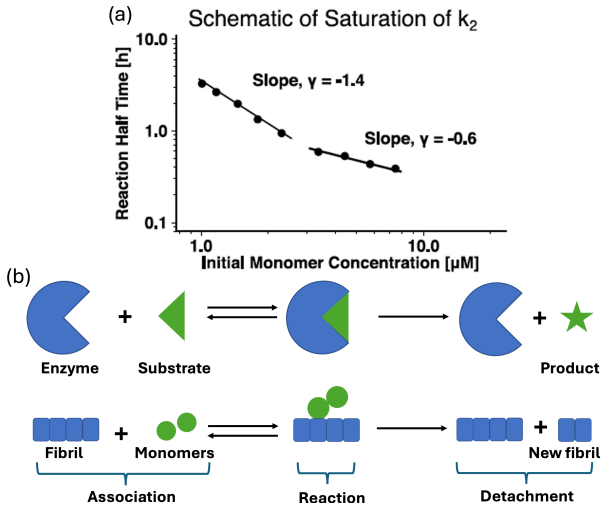

Figure 6: **a**: Schematic data for Aβ40 representing the saturation of the secondary nucleation at higher concentrations [57].**b**: Graphical depiction of the proposed reaction scheme for enzyme kinetics or secondary nucleation in amyloid formation.

ciation (binding of monomeric peptides to existing fibrils), reaction (rearrangement of monomers), and detachment (release of newly formed oligomers that may then continue to aggregate into larger amyloid fibrils) (Fig. 6). In this thesis, we mainly investigated the attachment and detachment steps of secondary nucleation, using Aβ40 and Aβ42 as model peptides.

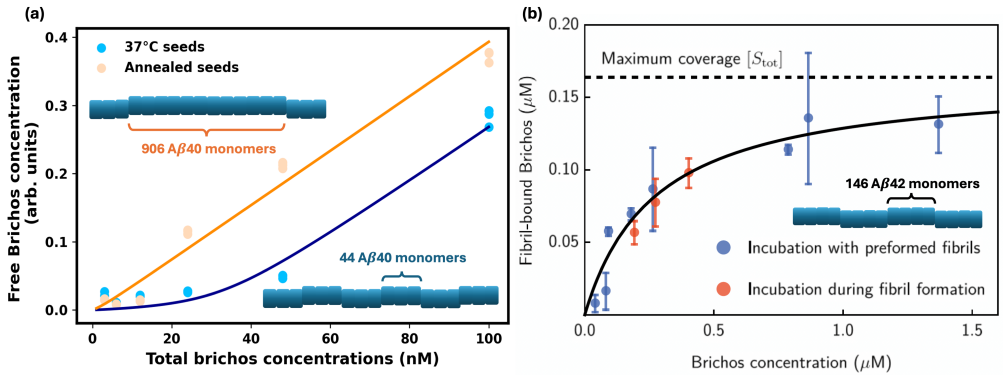

Figure 7: **a**: Solutions of 4.5 μM Aβ40 fibrils (annealed or 37°C) with 3 to 100 nM Alexa488-proSP-C Brichos are incubated for 2 h at 37 °C, and monitored by FCS to see the number of diffusing Alexa488-proSP-C Brichos. **b**: Binding of proSP-C Brichos to 24 μM Aβ42 fibrils monitored by MDS.

9.2 Arrival sites of secondary nucleation

In paper I, we investigated the sites of secondary nucleation using a system composed of Aβ42 or Aβ40 fibrils together with the proSP-C Brichos chaperone domain, a known secondary nucleation inhibitor [58] that is hereafter referred to as Brichos. In samples containing a fixed amount of Aβ40 fibrils, we incrementally added Alexa-488-labeled Brichos. The concentration of free Alexa-488-labeled Brichos in solution was measured by FCS and is shown as blue dots in Fig. 7(a). Most of the Brichos is bound to the Aβ40 fibrils at low concentrations of the chaperon domain. At higher concentrations of Brichos, the concentration of free Brichos in solution begins to increase until saturation is reached. These saturation conditions are here interpreted as the conditions where all secondary nucleation sites are occupied by Brichos. By fitting the blue data points in Fig. 7(a) using a standard ligand-protein 1 : 1 binding model, we determined the stoichiometry of Brichos versus Aβ40 monomers in fibrils. Assuming one Brichos binds to one secondary nucleation site, the average number of Aβ40 monomers between two secondary nucleation sites is approximately 44. Similarly, the binding of Brichos to Aβ42 fibrils was investigated. In these experiments, we traced Alexa labeled Brichos in the presence of Aβ42 fibrils using MDS. As shown in Fig. 7(b), the overall trends are the same as shown for Aβ40, with the concentration of fibril-bound Brichos increases with total Brichos concentration until saturation is reached. Fitting of this data yields a binding stoichiometry of 146 Aβ42 monomers per Brichos molecule. The results in Fig. 7 thus imply that secondary nucleation sites are rare on both Aβ40 and Aβ42 fibrils.

The finding that the secondary nucleation sites are rare on both Aβ40 and Aβ42

fibrils lead us to the hypothesis that secondary nucleation sites are defects along the fibril surface that form during fibril assembly process. To test this hypothesis, we aimed at annealing Aβ40 fibrils, in other words, largely eliminating defects, and test whether annealed fibrils' secondary nucleation sites are also eliminated. We tried an annealing approach commonly used for self-assembled systems based on controlling the kinetic pathway of self-assembly [59, 60]. In short, we lowered the rate of forming fibrils by decreasing supersaturation during Aβ40 aggregation process. The supersaturation level can be reduced by controlling the temperature during Aβ aggregation, since the solubility of Aβ40 increases from 37°C to 60°C, as shown by the red arrows in Fig. 8(a). Compared to Aβ40 fibrils generated at 37°C throughout aggregation (hereafter referred to as 37°C fibrils), annealed fibrils can be generated by decreasing the temperature from 60 to 37°C. To maintain the morphology of annealed fibrils consistent with fibrils formed at 37°C, we introduced 2% of 37°C fibrils at the start of the annealed fibril aggregation. Cryo-EM data confirmed no visible morphological differences between annealed fibrils and 37°C fibrils (Paper I).

To test if annealed fibrils differ with respect to the interaction with the Brichos chaperone domain, we conducted Brichos-fibrils binding experiments using FCS as described above. The binding data for annealed fibrils are shown as yellow dots in Fig. 7(a). The turnover point for annealed fibrils occurs at a lower total proSP-C Brichos concentration compared to 37°C fibrils. This suggests that annealed fibrils have fewer chaperone binding sites, indicating fewer sites available for secondary nucleation [58]. The fitted data confirmed that the number of Brichos binding sites is reduced by approximately 95% in annealed fibrils relative to fibrils formed entirely at 37°C.

We finally tested the seeding efficiency of annealed fibrils compared to 37°C fibrils using a ThT assay. As shown in Fig. 8(c) and (d), the aggregation of Aβ40 seeded by 2% or 40% annealed fibrils is slower than that seeded by 37°C fibrils. We were unable to fit the aggregation data with a kinetic model that uses fibril length as the only free variable to distinguish between the annealed and 37°C seeds. This misfit suggests that the decrease in elongation sites alone cannot explain the reduced seeding efficiency of annealed fibrils. However, the same kinetic data can be fitted by a model that varies the number of secondary nucleation sites between annealed and 37°C seeds. The fitting results indicate that annealed seeds have 92% fewer secondary nucleation sites than 37°C seeds, which broadly agrees with the 95% reduction estimated using proSP-C Brichos stoichiometry.

In conclusion, decreased supersaturation during Aβ40 aggregation results in reduced defect formation and, consequently, fewer secondary nucleation sites in

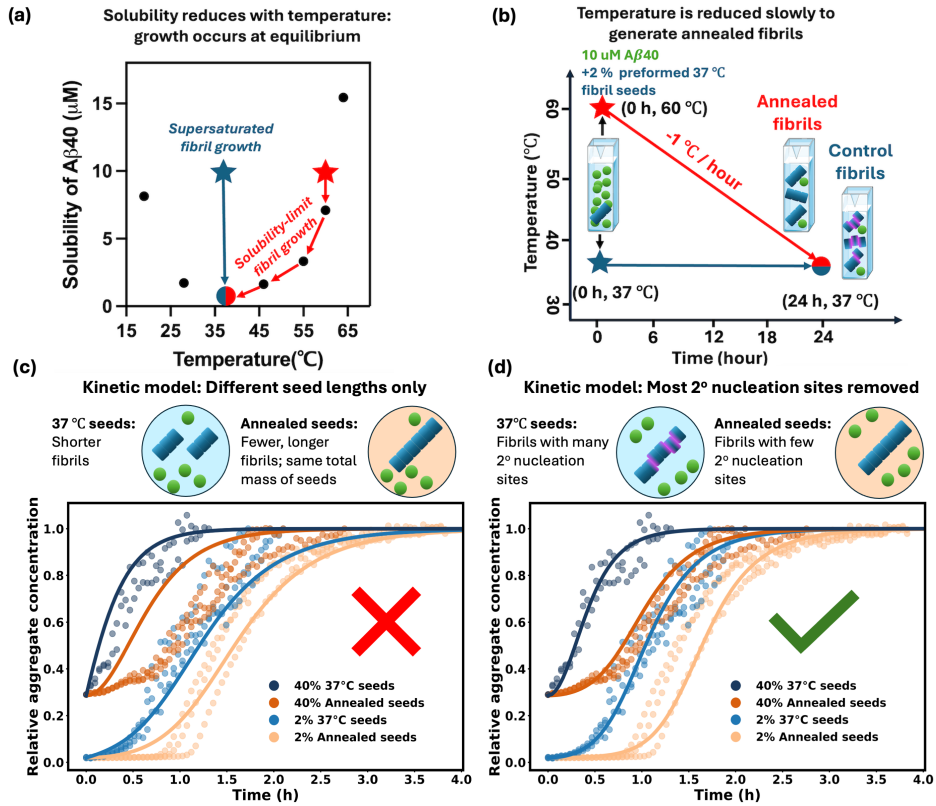

Figure 8: **a**: The solubility of Aβ40 at varying temperatures. The black data points are adapted from [61] **b**: we grow fibrils designed to be largely free of growth defects, by slowly reducing the temperature of a solution of initially slightly supersaturated monomeric Aβ40 from 60 to 37 °C by 1 °C per hour. **c** and **d**: The aggregation of 5 μM Aβ 40 with 2 or 40% annealed or 37 °C seeds was monitored by ThT in plate reader. The fitting (lines) assumed that the delayed aggregation of annealed seeds are due either to longer fibril length.

annealed fibrils.

9.3 Detachment of secondary nucleus from fibrils can be facilitated by shear force

In paper II, we observed accelerated aggregation of four amyloid proteins—IAPP, Aβ42, Aβ40, and tau (Paper II)—under mild agitation compared to idle conditions (data for IAPP adapted from [62]). These observations motivated a detailed study of how the mild agitation affects the different microscopic steps of the aggregation processes, including fragmentation, elongation, primary nucleation, and secondary nucleation in Aβ42 fibril formation.

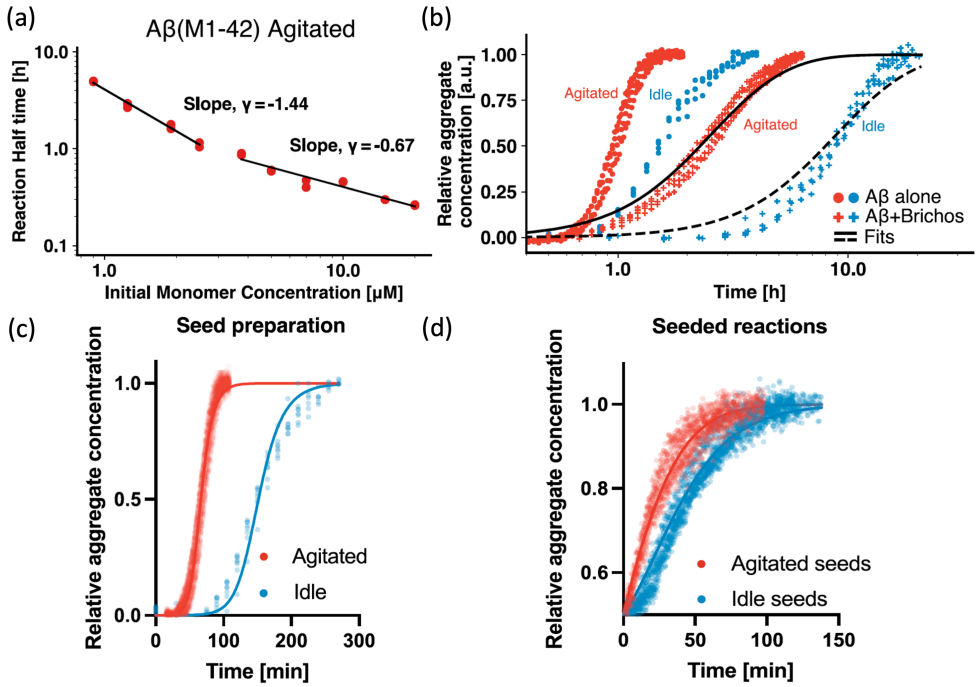

Figure 9: **a**: The double logarithmic plots of the data for Aβ42 under gentle agitation caused by continuous reading. **b**: Aggregation kinetics experiments in the absence and presence of a secondary nucleation inhibitor proSP-C Brichos. **c**: Aβ42 fibrils were formed from 2.5 μM Aβ42 monomers under agitated (red), and idle (blue) conditions. To test if elongation rate is accelerated by agitation, the resulting fibrils formed in reaction **c** were used to seed new reactions, after reaching the plateau. **d**: The seeded reactions were carried out at a 1:1 mass ratio of seed:monomer with a total Aβ42 concentration of 2.5μM. Both seeded reactions were carried out using a continuous reading frequency, in red with seeds made under agitation and in blue with seeds formed under idle conditions.

The effect of agitation on fragmentation was studied using the log-log plot of halftime versus initial monomer concentration, as shown in Fig. 9(a). The slope of linear fit to the data points at low initial monomer concentration is -1.4, which is characteristic of secondary nucleation-dominated Aβ42 aggregation as previously described (Fig. 6(a)). With increasing initial monomer concentration, the secondary nucleation sites on the fibrils become fully occupied with monomers, thus the slope increases. If accelerated Aβ42 aggregation were due to fragmentation, we would expect a negative curvature of the log-log plot with a slope of -0.5 at low concentrations and an even lower slope at high concentrations. This is because fragmentation rates are not monomer-dependent and dominate at low concentrations, whereas secondary nucleation becomes dominant at higher concentrations, leading to a lower slope.

After excluding the role of fragmentation, the remaining steps that could be responsible for the observed effect are primary nucleation, elongation and sec-

ondary nucleation. We followed the aggregation of Aβ42 with or without Brichos (the chaperone used to detect secondary nucleation sites in Paper I) under idle or agitated conditions. The concentration of added Brichos was high enough to render secondary nucleation negligible. As shown in Fig. 9(b), the aggregation of Aβ42 under both agitated and idle conditions is delayed by the addition of Brichos. However, the agitated samples still aggregate faster than the idle ones with the addition of Brichos, indicating that secondary nucleation alone cannot explain the accelerated aggregation.

We fitted the kinetic traces with Brichos using the primary nucleation-elongation model [19], giving the agitated Aβ42 a 12-fold higher k_+k_n product compared to the idle one. To decouple the effects of elongation and primary nucleation, we monitored the agitated aggregation of Aβ42 (Fig. 9(d)) with 50% seeds generated under either agitated or idle conditions (Fig. 9(c)). The results show that the agitated seeds accelerate the aggregation of Aβ42 more effectively than the idle seeds. Agitation would only produce longer fibrils if it primarily increased elongation, leading to fewer fibril ends and thus seeds with lower seeding efficiency. The opposite effect is shown in Fig. 9(d), indicating that the agitated seeds are shorter due to faster secondary nucleation rather than elongation.

We thus conclude that primary nucleation is responsible for the 12-fold increase in k_+k_n product. We fitted the aggregation data of Aβ42 with a concentration series, using a 12-fold increase in primary nucleation and a 4-fold increase in secondary nucleation for agitated conditions compared to idle ones (Paper II). The resulting fit describes the data well, implying that both primary and secondary nucleations are strongly affected by mild agitation.

In summary, our findings indicate that the acceleration of aggregation under gentle agitation is due to the combined effects of primary and secondary nucleation. Consequently, we anticipate an increased production of oligomers during agitated aggregation, as these oligomers defined as the intermediate between monomers and fibrils arise from both nucleation pathways. We measured the concentration of Aβ42 oligomers under idle and agitated conditions at the half-time of aggregation using the liquid-electrode microchip free-flow electrophoresis device. The timepoint corresponding to the halft-time of the aggregation was chosen since the oligomer concentration has previously been found to peak around this stage of the reaction [25]. The liquid-electrode microchip free-flow electrophoresis device utilizes the same confocal microscope and laminar flow setup as described for MDS described in the methods section. Additionally, it incorporates electrophoresis to enhance the separation of oligomers from monomers and fibrils. As shown in Fig. 10(c), the average photon count distribution of the agitated sample peaked at a higher channel position compared

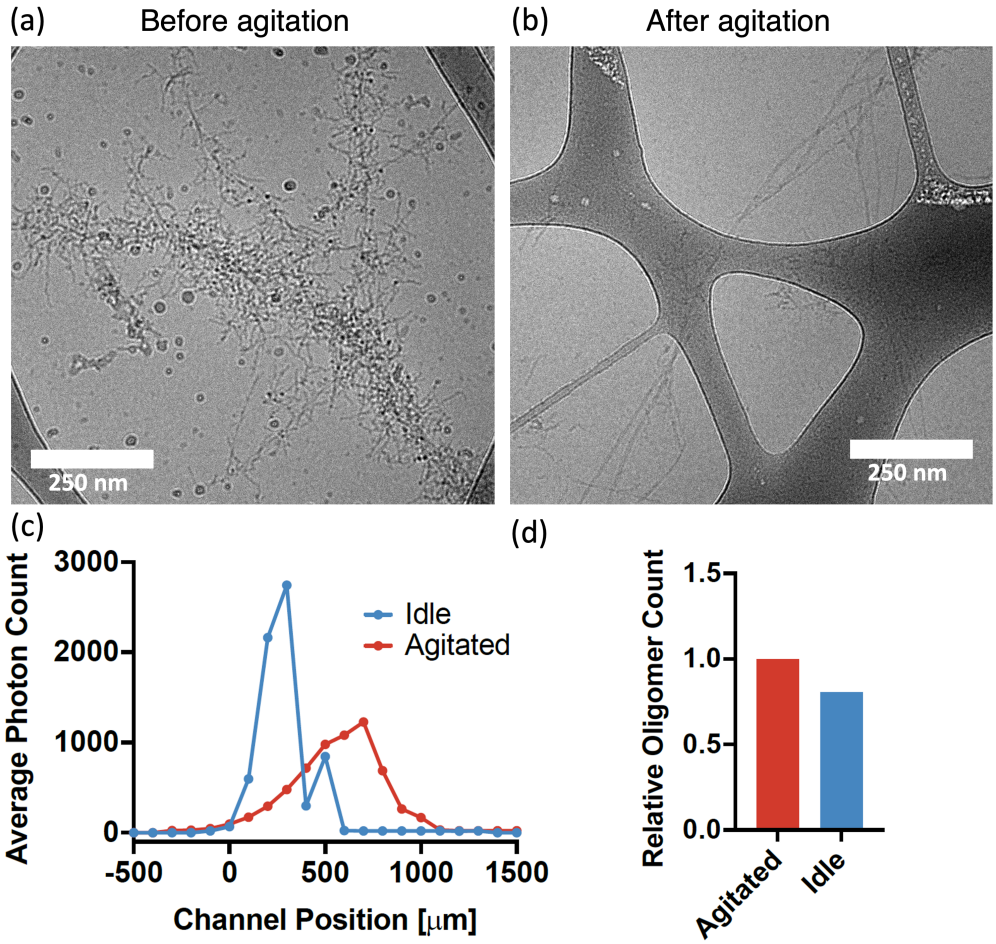

Figure 10: **a**: cryo-TEM images of fibrils formed in a solution of 13 μM Aβ42 at pH 6.8, 37 $^{\circ}$C incubated for around 6 h. Fibrils formed in this idle condition are densely covered by protrusions. **b**: The solution was agitated for one minute (using a vortex) and imaged again. The protrusion density at the fibril surface was significantly reduced by mechanical agitation. **c**: Average photon count versus chamber position of species measured for idle (blue) and agitated (red) conditions. **d**: Relative oligomer count at $t_{1/2}$ for idle (blue) and agitated (red) samples.

to the idle sample. Higher channel positions correspond to larger average-sized species, except for fibrils, which tend to be at lower channel positions, possibly due to orientation perpendicular to the electric field. Then, by counting the fluorescent events exceeding the brightness of 2 monomers and below the threshold fluorescence of a fibril, we can compare the population of oligomers in agitated and idle samples. As shown in Fig. 10(d), gentle agitation leads to more oligomers at the half-time compared to idle conditions. The increased oligomer presence in agitated samples can be attributed to two factors: firstly, agitation enhances the detachment of nuclei formed via secondary nucleation on

amyloid fibrils; secondly, it accelerates primary nucleation, directly generating oligomers.

We finally hypothesized that agitation can accelerate secondary nucleation by increasing shear forces, which facilitate the detachment of newly formed aggregates from fibril surfaces. To test this hypothesis, we imaged Aβ42 fibrils decorated with protrusions, interpreted as intermediates of secondary nucleation (Fig. 10(a)). These decorated fibrils were formed under idle conditions following procedures described in a previous study [63]. The solution containing the decorated fibrils was then agitated and imaged again, showing fewer decorated fibrils (Fig. 10(b)). These cryo-TEM results suggest that agitation decreases the presence of Aβ42 aggregates branching from fibril surfaces, which are likely secondary nuclei. The less decorated fibrils after agitation will further lead to larger amounts of exposed secondary nucleation sites, thereby accelerating secondary nucleation more efficiently compared to fibrils formed under idle conditions.

In conclusion, from the combined observations on secondary nucleation in paper I and II, it is proposed that the secondary nucleation sites are defects during formation of fibrils, and the detachment of nucleus from the the secondary nucleation sites can be facilitated by shear force.

10 Formation of Aβ and GM1 co-assemblies

10.1 Co-assemble of Aβ40 or Aβ42 and GM1 in micellar aggregates

Having investigated on the self-assembly of Aβ, we are interested in the effect of GM1 micelles on Aβ aggregation. In paper III, we revealed the co-assembly of Aβ42 monomers with GM1 in micellar aggregates using MDS. Both MDS and FCS can measure the diffusion of fluorescently labeled species, thereby providing an estimate of the hydrodynamic radius, r_H, of the labeled species (assuming spherical shape). In paper III, we mixed a small amount of Alexa647-Aβ42 with varying amounts of unlabeled GM1 (GM1/Aβ ratios between 600-50000) and measured the samples by means of MDS shortly after mixing. The concentration of Alexa647-Aβ42 was kept low to avoid amyloid formation. The results are plotted as blue dots in Fig. 11(a). With increasing concentrations of GM1, the average r_H of Alexa647-Aβ42 increases to a stable value of around 6 nm. The red dots in the same figure represent samples with pure GM1, with the hydrophobic probe NBD-PE dissolved in the micelles. The average r_H of

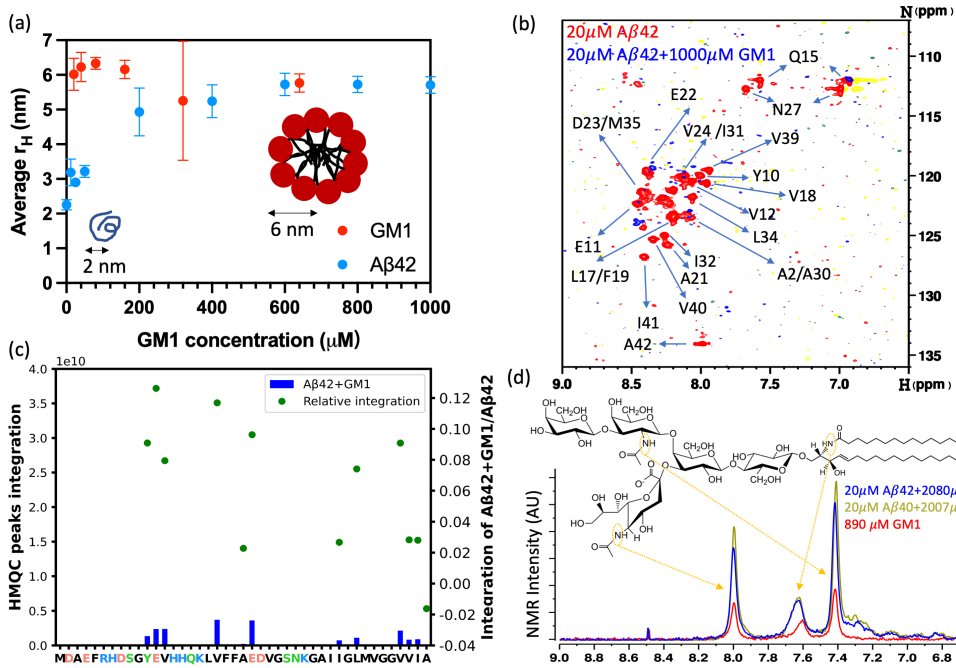

Figure 11: **a**: The average hydrodynamic radius of 20 nM Alexa647-Aβ42 in the absence and presence of 12-1000 μM unlabelled GM1 (blue) and of 12-1000 μM GM1 containing 0.5 mol% NBD-PE (red) is plotted as a function of GM1 concentration. The cartoons are schematic illustrations of Aβ monomer and GM1 micelle. **b**: Aβ42 with and without GM1 by means of HSQC NMR. **c**: Integrated intensities of HMQC peaks for 20μM Aβ42 and 1000μM GM1. The relative integration calculated by dividing the integration of Aβ42 and GM1 sample by the integration of 20μM pure Aβ42 sample is plotted as green dots. The x axis with red, blue, green, and black denotes negatively charged residues, positively charged residues, polar neutral residues, and non-polar residues, respectively. **d**: Three GM1 amine group peaks shown in the ^{1}H NMR spectrum. Among the ^{1}H NMR peaks of GM1 amine groups, the ^{1}H in sphingosine amine is shifted with addition of Aβ42 or Aβ40.

NBD-PE-labeled species remains almost unchanged at a value of around 6 nm across different lipid concentrations, consistent with the reported size of GM1 micelles [14]. This r_H is also similar to the stable average r_H of Aβ42 at high lipid-to-peptide ratios shown by the blue dots, suggesting that Aβ42 and GM1 form micellar co-assemblies.

Next, we characterized the co-assemblies formed by GM1 together with either Aβ42 and Aβ40 using NMR spectroscopy, which provides atomic-level information on peptide-lipid interactions. In these studies, we used samples with lower lipid-to-peptide ratios, as the concentration of Aβ needs to be at least 1000 times higher in NMR than in MDS, while too high GM1 concentrations may lead to the formation of other lipid structures than spherical micelles. We acquired a ^{1}H-^{15}N HMQC spectrum of freshly purified ^{15}N-labeled Aβ42, shown as red peaks in Fig. 11(b). Each red peak represents a correlation between ^{1}H and ^{15}N nuclei in a specific chemical environment, which can be assigned to the

amide groups of particular amino acids. The assignment of Aβ42 HMQC peaks is provided in the supplementary information of Paper IV. We also recorded the HMQC spectrum of freshly purified ^{15}N-labeled Aβ42 mixed with 50 times more unlabeled GM1, shown as blue peaks in the same figure. We observed fewer and lower intensity peptide peaks in the samples that also contain GM1 as compared to pure Aβ42. Such reduction in intensity can be due to changes in both the chemical environment and the Aβ42 dynamics. In paper IV, we analysed the NMR data for both GM1 and Aβ at different temperatures, and proposed the observed changes in peptide signal is due to Aβ embedded within peptide-lipid co-assemblies.

For a more detailed analysis, we integrated the HMQC peaks from peptide in the presence and absence of GM1 (represented by red and blue peaks in Fig. 11(c)) and plotted their relative intensities (green dots). From this analysis, we aim to visualize the change in HMQC signals for each assigned amino acid due to the addition of GM1. The green dots in Fig. 11(c) show a trend of decreasing relative intensity towards the C-terminus of Aβ42, which is more hydrophobic compared to the N-terminal region. Similar trend is seen for Aβ40 (SI figure in paper IV). Additionally, the relative intensity drops below 0.04 for Alanine 21, Isoleucine 32, Valine 40, Isoleucine 41, Alanine 42, all of which are hydrophobic.

Finally, the influence of Aβ42 or Aβ40 on the GM1 was monitored in the ^{1}H NMR spectra from samples containing GM1 with or without Aβ. The three amide groups of GM1 are assigned in Fig. 11(d), with the middle peak representing the sphingosine amine located at the junction between the GM1 head group and the hydrophobic chains. We observe a change in the chemical shift of the sphingosine amine upon the addition of Aβ, which may indicate the insertion of Aβ into the head group-tail region of in the micellar co-assemblies. Based on the previous analysis of relative intensities, the hydrophobic regions of Aβ are likely more embedded within the hydrophobic core formed by GM1 tails, which also make sense from a molecular perspective.

10.2 Aβ42 distribution between micelles

It has previously been observed for other membrane-active amyloid-forming proteins (i.e. α-synuclein[64] and IAPP[65]) that the proteins associate with lipid membranes with positive cooperativity, meaning that it is energetically favorable to adsorb to a patch that already contains protein compared to an empty spot at the membrane. Inspired from these studies, we here raised the question if also the association of Aβ with GM1 is cooperative. The accumulation of multiple peptides within a few micelle might in turn promote peptide aggregation. Thus,

we examined whether there is preferential (positively cooperative) association of Aβ42 with micelles that already contain peptides, or if the peptide distributes randomly across all micelles. To address this question, we used samples with a low amount of Alexa647-Aβ42 in the presence of an excess of GM1 micelles (micelle/Aβ42 ratio around 19–38), meaning that if the peptide is randomly distributed, each micelles will on average contain one or zero peptides. If we had instead used samples with low lipid-to-peptide ratios, the micelles might contain more than one Aβ molecule on average, making it difficult to distinguish between random distribution and cooperative association.

As shown in Fig. 12(a), the count rate of Alexa647-Aβ42 in the presence of unlabeled GM1 was recorded for 120 seconds, with each spike representing one fluorescently labeled species passing through the confocal detector. The count rate is positively correlated to the number of Alexa647-Aβ42 molecules within a single species. We plotted the number of spikes against their normalized count rate to show the distribution of species containing different amounts of Alexa647-Aβ42. As shown in Fig. 12(b), the majority of spikes have a low normalized count rate, indicating that most fluorescent species in the peptide-lipid mixture contain a low amount of Alexa647-Aβ42. The occurrence and intensity of the spikes from the sample containing pure Alexa647-Aβ42 are similar to that of the Alexa647-Aβ42 and unlabeled GM1 mixture, suggesting that the distribution of Alexa647-Aβ42 remains monomeric in the presence of excess GM1 micelles. Furthermore, we did not observe any FCS-FRET signal between Alexa647-Aβ42 and Alexa488-Aβ42, with or without unlabeled GM1 (Paper IV). These FCS and FCS-FRET results suggest that the peptide is randomly and uniformly distributed across all micelles, with only one (or zero) peptide per micelle, meaning no signs of peptide accumulation in some of the micelles.

10.3 Co-assembly of Aβ and GM1 in amyloid aggregates

In paper III, we also discovered the co-assembly of Aβ42 with GM1 after amyloid formation using cryo-TEM and confocal microscopy. Samples containing Aβ42 and GM1 micelles were incubated at 37°C for 5 days, then imaged using cryo-TEM (Fig. 13(a)). We observed some fibrils decorated by micelles, indicated by white arrows and highlighted as magenta lines decorated with green dots in Fig. 13(a). The fibrils exhibit the same morphology as pure Aβ42 fibrils, and the micelles are of similar shape and size as pure GM1 micelles (Paper III). Decorated fibrils were also observed in samples containing Aβ40 and GM1 incubated for 7 days (Fig. 13(b)). The cryo-TEM imaging only provides information on aggregate morphology. Therefore, we here combined the cryo-TEM experiments

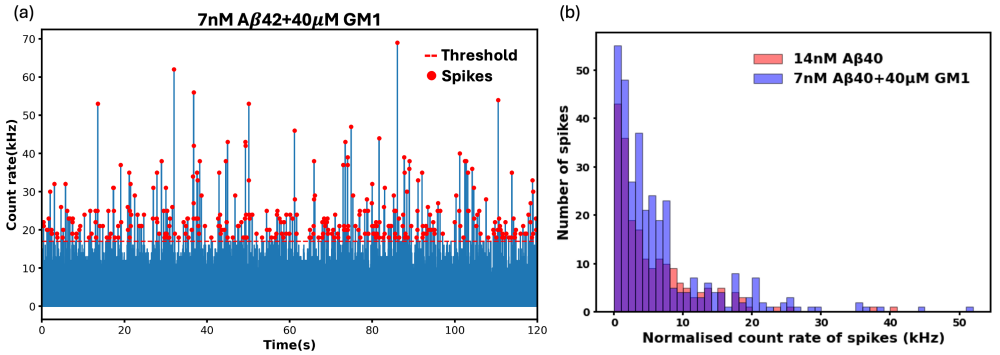

Figure 12: **a**: Count rate of Alexa647-labeled Aβ42 mixed with non-labeled GM1 was measured by FCS for 120 seconds. The threshold for spikes is set as the average count rate plus six standard deviations. **b**: Number distribution of spikes count rate measured from Alexa647-labeled Aβ42 with or without non-labeled GM1. The count rate is normalised by subtracting threshold for better comparison.

with fluorescent microscopy to obtain information on the location of the different chemical components, although at a lower spatial resolution. In order to detect amyloid fibrils and GM1 mcielles, we used pFTAA to detect amyloid fibrils and Atto-DPPE dissolved in the GM1 micelles. As shown in Fig. 13(c) and (d), the green pFTAA-labeled species co-localize with the red Atto-DPPE-labeled species, indicating the colocalization of Aβ42 fibrils and lipids. Similarly, the colocalization of Aβ40 fibrils and GM1 micelles is also shown (Paper III). In conclusion, both cryo-TEM and confocal microscopy images reveal the co-assembly of GM1-rich micelles with both Aβ40 and Aβ42 amyloid fibrils.

10.4 Aβ-GM1 co-assembly influence on peptide solubility

The formation of Aβ-GM1 co-assemblies can influence the apparent solubility of Aβ, thereby altering the driving force for peptide aggregation. We measured the apparent solubility of Aβ by incubating samples containing Aβ40 or Aβ42 with varying amounts of lipids for at least 3 days. The time was chosen to ensure that the aggregation reaction is completed. The measured concentration was then compared to the solubility of the pure peptides after the aggregation reaction has been completed. In order to separate the fibrils from the solution, the samples were centrifuged at the same temperature as incubation (37°C), and the supernatant was collected for HPLC-MS analysis. We integrated the peak intensity of m/z (mass/charge ratio) corresponding to Aβ40 or Aβ42 over the elution time. The integrated peak intensities are plotted against the lipid-to-peptide ratio, as shown in Fig. 14(a). With an increasing lipid-to-peptide ratio, the intensity from both Aβ42 and Aβ40 increases. The measured intensity is

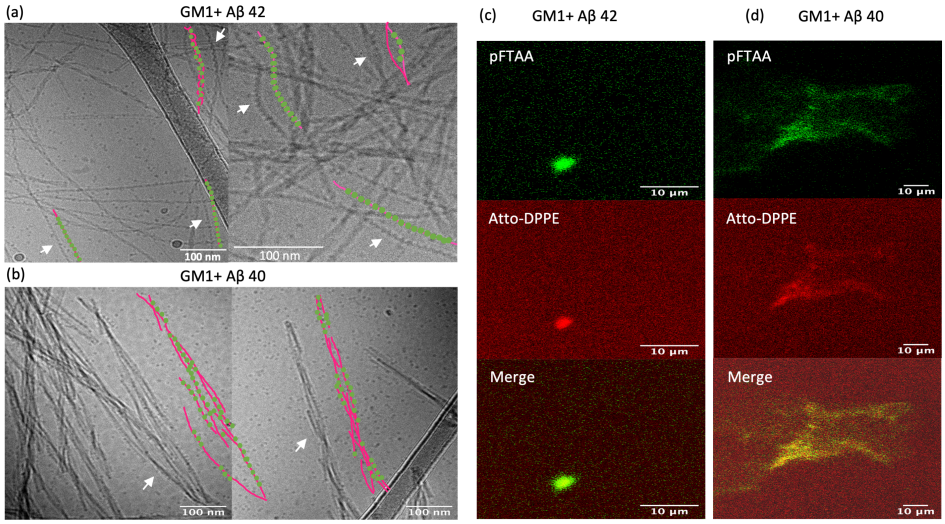

Figure 13: **a**: cryo-TEM images of fibrils formed in a solution with the mixture of 800 μM GM1 (containing 8 μM Atto-DPPE) and 5 μM Aβ42 after 5 days incubation. **b**: cryo-TEM images of fibrils formed in a solution with the mixture of 500 μM GM1 and 3 μM Aβ40, incubated for 7 days. In panels a and b we have added our interpretation of a few features as cartoons with magenta indicating fibrils and green indicating micellar decorations of the fibrils. **c**: Confocal microscopy images of solutions containing 800 μM GM1 and 5 μM Aβ42, incubated for three days. **c**: Confocal microscopy images of solutions containing 800 μM GM1 and 5 μM Aβ40, incubated for 7 days. pFTAA (0.75 μM, green) is used to detect aggregated peptide, and Atto-DPPE (4 μM, red) is used to detect GM1 micelles, merged images from green and red channel shows a co-localization of pFTAA and Atto-DPPE.

positively correlated with the concentration of the peptide until it reaches a point of saturation.

The results in Fig. 14(a) suggest that the concentration of Aβ in the supernatant above the amyloid fibrils is higher at increasing lipid-to-peptide ratios. Another finding from Fig. 14(a) is that the signal measured for Aβ40 is approximately 10 times higher than that of Aβ42 at the same lipid-to-peptide ratio, consistent with previous findings that the solubility of Aβ40 is around 10 times higher than that of Aβ42 [24].

In a complementary experiment in paper IV, we instead studied the apparent solubility of Aβ40 by diluting fibrils in either pure buffer or buffer containing GM1. The samples were incubated for up to 10 days. The diluted samples were centrifuged and analyzed by HPLC-MS at different time points, as described above. The results are shown in Fig. 14(b). At the start of the incubation, there was not or only very little peptide detected in the supernatants. However, over time, significantly more peptide was dissolved to the GM1 solution compared to the buffer solution, particularly after 4 and 10 days. These fibril-dissolution results are consistent with the monomer-GM1 incubation results, suggesting

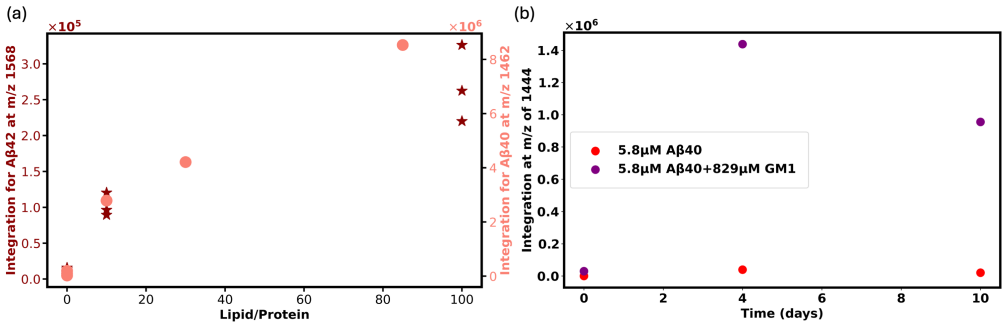

Figure 14: **a**: Integration of HPLC-MS intensities for peptide over time is plotted against GM1/Aβ ratios. **b**: Samples containing 58μM Aβ40 fibrils were diluted 10 times by adding either buffer alone or buffer with 1746μM GM1. The supernatant from the diluted samples were analysed by HPLC-MS, and the intensities of the Aβ40 peaks are plotted against the time after dilution.

that GM1 can increase the apparent solubility of both Aβ40 and Aβ42.

The co-assembly between Aβ monomers and GM1 micelles most likely contribute to the increased apparent solubility of Aβ upon the addition of GM1. The concentration of Aβ in solution here include both free Aβ and Aβ co-assembled with GM1 micelles. Assuming equilibrium is reached, then the chemical potential of Aβ should be the same in all phases, here including Aβ in fibrils, Aβ monomers in solution and Aβ in micelles. Assuming the chemical potential of Aβ in fibrils is not changed by the presence of GM1, the chemical potential the Aβ monomers in solution should also remain unchanged. The observed increase in apparent solubility by GM1 is therefore most likely due to the solubilization of Aβ in GM1 micelles. This scenario is similar to the case where Aβ is solubilized by chaperones in micelle-like aggregates [66, 67], where the apparent solubility of Aβ is increased by the presence of a chaperone.

10.5 Aβ-GM1 co-assembly influence on peptide kinetics

In papers III and IV, we also studied the influence of GM1 on the kinetics of Aβ aggregation. In paper IV, we analyzed the sum of the HMQC integrated peak intensity over all peaks originating from peptide and studied how this total intensity varied over time. We observed a decrease in HMQC integrated peak intensities over time for all samples containing Aβ40 (Fig. 15(a)), which is due to the aggregation of monomers into fibrils, where the latter are not detectable by HMQC spectroscopy. For samples containing a mixture of Aβ40 and GM1, the rate of HMQC signal decrease is smaller compared to pure Aβ40, indicating that GM1 delays the aggregation of Aβ40. Another observation from this figure

is that the final stable value of integrated peak intensity is higher for samples with GM1 compared to the pure peptide samples. The HMQC integrated peak intensity for samples containing both Aβ and GM1 might be attributed to free Aβ monomers as well as monomers in co-assemblies, as the radius of the co-assemblies is only about three times larger than Aβ monomers. This observation suggests that the apparent solubility of Aβ40 is higher at higher lipid-to-peptide (L/P) ratios, which is consistent with the above described HPLC-MS results (Fig. 14).

In the studies of Aβ42 aggregation, we took a different approach and monitored the aggregation processes by means of the p-FTAA fluorescence intensity. The reason for this was that the HMQC signal from the Aβ42-GM1 samlpes was too low to enable us to follow the aggregation reaction. p-FTAA is the fibril-sensitive dye we used for confocal images in a previous section. In Fig. 15(b), the p-FTAA intensity of pure Aβ42 samples increases over time until it reaches a stable level, representing the accumulation of fibrils over time until equilibrium. In the presence of GM1, the Aβ42 fibril formation is delayed, and this delay is more pronounced at higher GM1-to-Aβ42 ratios. It is difficult to obtain direct information on apparent solubility from these experiments as also other factors than the total amount of fibrils can influence the measured p-FTAA signal, *e.g.,* bundling of fibrils or fibrils decorated by micelles that scatter lights [68].

The changes in apparent solubility is one out of several factors that may lead to changes in peptide amyloid aggregation. In order to study how GM1 micelles affect the different kinetic steps of the aggregation reaction, we investigated a set of conditions in paper III, including seeded reactions and varying lipid-to-peptide ratios. In these experiments, peptide concentration was set to 3 μM instead of the higher concentration of 20 μM as used in paper IV. We incubated 3 μM Aβ40 or Aβ42 with 0%, 1%, or 25% seeds in the presence of varying amounts of GM1 (Fig. 15(c) and (d)). In conditions of light seeding, the primary nucleation of Aβ is bypassed. In conditions of heavy seeding, both primary and, to a large extent, secondary nucleation are bypassed. From the aggregation curves, monitored by pFTAA (Fig 4 and 5, paper III), we extracted the relative halftime for the aggregation reactions. These values were normalized to the halftime of Aβ aggregation without GM1 and plotted for different lipid to peptide ratios in Fig. 15(c) and (d).

For unseeded Aβ40, the relative halftime increases with higher lipid-to-peptide ratios. GM1 is also observed to delay aggregation in both lightly and heavily seeded Aβ40 reactions.The influence of GM1 on Aβ40 aggregation kinetics is consistently characterized by retardation across different initial Aβ monomer or seed concentrations. There are several microscopic aggregation steps that may

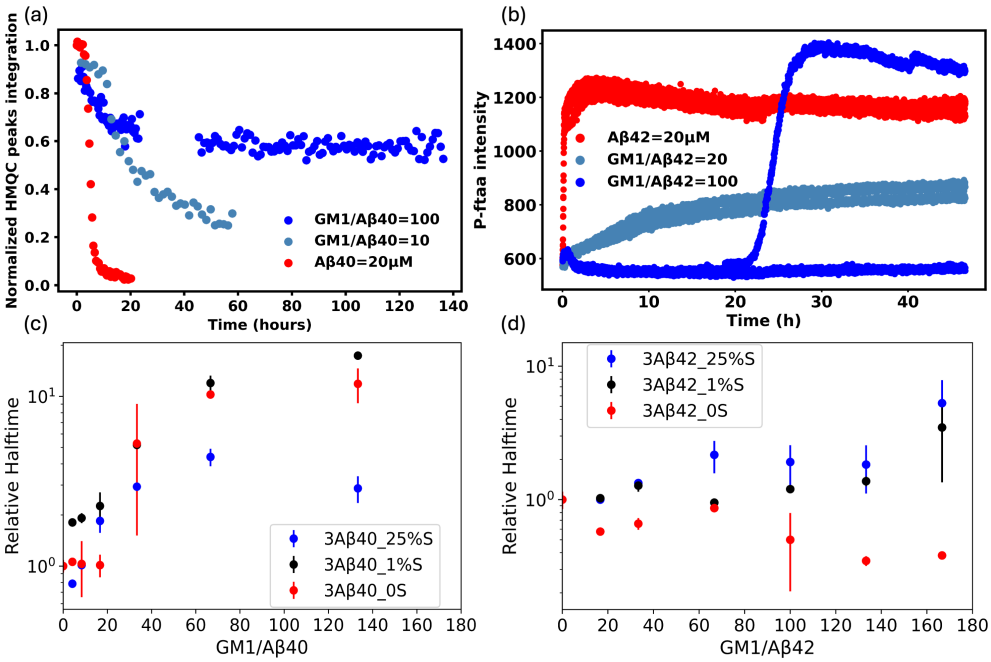

Figure 15: **a**: Integrated intensity of HMQC peaks of ^{15}N-labeled Aβ40 with different amount of GM1 were taken at different time points. The sum of all HMQC peaks in a single spectrum is plotted against time. The HMQC peaks are normalised by the signal at the first time point. **b**: The p-FTAA intensity is plotted against time for samples containing 20μM Aβ42 and different amount of GM1. The p-FTAA concentration is 1.5μM in all these three samples. **c** or **d**: Relative halftime extracted from kinetic curves in paper III plotted against GM1/Aβ40 or GM1/Aβ42 ratio, respectively.

be influenced by the addition of GM1. Firstly, GM1 may retard all nucleation and growth processes, as peptide monomers are depleted from the solution into the GM1-Aβ co-assemblies, reducing the monomer concentration available for all aggregation reaction steps. Secondly, coating the fibril surface by GM1-containing assemblies may impact all processes occurring at the fibril surface, including secondary nucleation and elongation. The latter scenario is consistent with the seeding experiments, where Aβ40 aggregation is delayed even when the primary or secondary nucleation is bypassed. In addition, micelles may also interact with oligomers although not studied in detail here.

It is finally noted that the total Aβ42 peptide concentration appears to have a rather strong effect on the observed effects of GM1. The aggregation of unseeded Aβ42 is accelerated by the addition of GM1 at peptide concentration of 3 μM (Fig. 15(d)), while we observe retardation at the same L/P ratio at peptide concentration of 20 μM, as shown in Fig. 15(b). When 1% or 25% Aβ42 seeds are added, GM1 again delays the aggregation of Aβ42 (Fig. 15(d)).

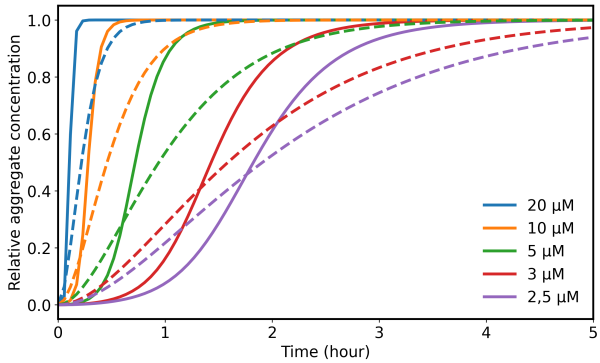

Figure 16: Secondary nucleation dominated model of the relative aggregate concentration plotted against time for 2.5 to 20 μM Aβ42. The dotted lines are with 100 times higher primary nucleation rate constant, combined with 10 times lower secondary nucleation and elongation rate constants.

The different effects of GM1 on Aβ42 at low and high initial peptide concentrations can be attributed to several factors. The acceleration effect of GM1 is observed only in unseeded samples, indicating that only primary nucleation of Aβ is accelerated, while elongation and secondary nucleation may be retarded. We modeled secondary nucleation-dominated aggregation of Aβ42 at different initial concentrations using amylofit (Fig. 16). To simulate the effect of adding GM1, we increased the primary nucleation rate constant by 100-fold and reduced the elongation and secondary nucleation rates by 10-fold each. The resulting aggregation curves are shown as dotted lines. With higher initial Aβ concentrations, the delaying effect is more prominent. In addition, we cannot exclude that there is effects caused by the adsorption of the surface-active peptide and lipid, which can be different between the different experimental set-ups and concentrations. This may slightly skew the proportions between peptide and lipids, especially in samples with peptide concentrations.

Conclusions and outlook

Conclusions: In **Paper I**, it was found that secondary nucleation sites on Aβ40 and Aβ42 fibrils are rare and likely associated with core defects in the fibril structure. Reducing these defects by reducing supersaturation during fibril formation can greatly diminish Aβ40 secondary nucleation sites and rates, while preserving overall fibril morphology. In **Paper II**, it was found that mild agitation accelerates both primary and secondary nucleation steps in Aβ42 fibril formation, while elongation and fragmentation remained unaffected. Cryo-EM images showed that the detachment of aggregates from fibril surfaces is facilitated by agitation, likely due to the shear force generated by agitation. In **Paper III**, it was found that Aβ42 partition into GM1 micelles, forming co-assemblies. We also found Aβ42 and Aβ40 fibrils decorated by micellar-like aggregates, most likely are formed by GM1 lipids. GM1 influeces the kinetic of both un-seeded and seeded kinetics of Aβ42 and Aβ40 aggregation. In **Paper IV**, it was found that both Aβ42 and Aβ40 was solubilized by GM1 micelles. There are no indication of preferential association of Aβ42 to the micelles that already contain peptide. The Aβ42 and Aβ40 are likely localized both in the hydrophobic core and in the interfacial head group layer of the micelles. The co-assembly with GM1 increases the apparent solubility of Aβ42 and Aβ40, and retards the fibril formation process. **Outlook: Paper I:** Can other amyloid fibrils such as alpha-synuclein, tau, and IAPP be annealed as well? **Paper I:** Can we test the mechanical strength difference between defective and non-defective fibrils, by AFM or fragmentation? **Paper II:** Can we quantify the shear force, and test the influence on secondary nucleus accordingly? **Paper III and IV:** What is the exchange rate between peptide inside and outside of the co-assemblies? **Paper III and IV:** Can other micelle-forming lipids or amphiphiles dissolve amyloid proteins? **Paper III and IV:** How are oligomers influenced by the formation of peptide-lipid co-assemblies? **Paper III and IV:** What is the neurotoxicity of micelle-solubilized Aβ compared to pure Aβ?

11 References

[1] Mark A Findeis. The role of amyloid β peptide 42 in alzheimer's disease. *Pharmacology & therapeutics*, 116(2):266–286, 2007.

[2] Jun Wang, Ben J Gu, Colin L Masters, and Yan-Jiang Wang. A systemic view of alzheimer disease—insights from amyloid-β metabolism beyond the brain. *Nature reviews neurology*, 13(10):612–623, 2017.

[3] Alex E Roher, Chera L Esh, Tyler A Kokjohn, Eduardo M Castaño, Gregory D Van Vickle, Walter M Kalback, R Lyle Patton, Dean C Luehrs, Ian D Daugs, Yu-Min Kuo, et al. Amyloid beta peptides in human plasma and tissues and their significance for alzheimer's disease. *Alzheimer's & Dementia*, 5(1):18–29, 2009.

[4] Piotr Lewczuk, Jens Wiltfang, Johannes Kornhuber, and Anneleen Verhasselt. Distributions of aβ42 and aβ42/40 in the cerebrospinal fluid in view of the probability theory. *Diagnostics*, 11(12):2372, 2021.

[5] Niklas Mattsson, Philip S Insel, Susan Landau, William Jagust, Michael Donohue, Leslie M Shaw, John Q Trojanowski, Henrik Zetterberg, Kaj Blennow, Michael Weiner, et al. Diagnostic accuracy of csf ab42 and florbetapir pet for alzheimer's disease. *Annals of clinical and translational neurology*, 1(8):534–543, 2014.

[6] Charles Duyckaerts, Benoît Delatour, and Marie-Claude Potier. Classification and basic pathology of alzheimer disease. *Acta neuropathologica*, 118:5–36, 2009.

[7] Conny Leistner, Martin Wilkinson, Ailidh Burgess, Megan Lovatt, Stanley Goodbody, Yong Xu, Susan Deuchars, Sheena E Radford, Neil A Ranson, and René AW Frank. The in-tissue molecular architecture of β-amyloid pathology in the mammalian brain. *Nature Communications*, 14(1):2833, 2023.

[8] Wojciech Michno, Patrick M Wehrli, Henrik Zetterberg, Kaj Blennow, and Jörg Hanrieder. Gm1 locates to mature amyloid structures implicating a prominent role for glycolipid-protein interactions in alzheimer pathology. *Biochimica et Biophysica Acta (BBA)-Proteins and Proteomics*, 1867(5):458–467, 2019.

[9] Kelly L Wormwood Moser, Gregory Van Aken, Daniel DeBord, Nathan Galen Hatcher, Laura Maxon, Melissa Sherman, Lihang Yao, and Kim Ekroos.

High-defined quantitative snapshots of the ganglioside lipidome using high resolution ion mobility slim assisted shotgun lipidomics. *Analytica Chimica Acta*, 1146:77–87, 2021.

[10] Simonetta Sipione, John Monyror, Danny Galleguillos, Noam Steinberg, and Vaibhavi Kadam. Gangliosides in the brain: physiology, pathophysiology and therapeutic applications. *Frontiers in neuroscience*, 14:572965, 2020.

[11] Shelli L Frey and Ka Yee C Lee. Number of sialic acid residues in ganglioside headgroup affects interactions with neighboring lipids. *Biophysical journal*, 105(6):1421–1431, 2013.

[12] D Fennell Evans and Håkan Wennerström. The colloidal domain: where physics, chemistry, biology, and technology meet. 1999.

[13] Luis A Bagatolli. *Life-as a Matter of Fat-Lipids in a Membrane Biophysics Perspective*. Springer, 2015.

[14] Enamul Haque Mojumdar, Carl Grey, and Emma Sparr. Self-assembly in ganglioside–phospholipid systems: the co-existence of vesicles, micelles, and discs. *International Journal of Molecular Sciences*, 21(1):56, 2019.

[15] Marie Grey, Christopher J Dunning, Ricardo Gaspar, Carl Grey, Patrik Brundin, Emma Sparr, and Sara Linse. Acceleration of α-synuclein aggregation by exosomes. *Journal of Biological Chemistry*, 290(5):2969–2982, 2015.

[16] Khavinet Lourvanij. *Partial dehydration of glucose to oxygenated hydrocarbons in molecular-sieving catalysts*. Oregon State University, 1995.

[17] Domenico Acquotti and Sandro Sonnino. Use of nuclear magnetic resonance spectroscopy in evaluation of ganglioside structure, conformation, and dynamics. In *Methods in enzymology*, volume 312, pages 247–272. Elsevier, 2000.

[18] Therése Klingstedt, Andreas Åslund, Rozalyn A Simon, Leif BG Johansson, Jeffrey J Mason, Sofie Nyström, Per Hammarström, and K Peter R Nilsson. Synthesis of a library of oligothiophenes and their utilization as fluorescent ligands for spectral assignment of protein aggregates. *Organic & biomolecular chemistry*, 9(24):8356–8370, 2011.

[19] Georg Meisl, Julius B Kirkegaard, Paolo Arosio, Thomas CT Michaels, Michele Vendruscolo, Christopher M Dobson, Sara Linse, and Tuomas PJ

Knowles. Molecular mechanisms of protein aggregation from global fitting of kinetic models. *Nature protocols*, 11(2):252–272, 2016.

[20] Georg Meisl, Xiaoting Yang, Erik Hellstrand, Birgitta Frohm, Julius B Kirkegaard, Samuel IA Cohen, Christopher M Dobson, Sara Linse, and Tuomas PJ Knowles. Differences in nucleation behavior underlie the contrasting aggregation kinetics of the aβ40 and aβ42 peptides. *Proceedings of the National Academy of Sciences*, 111(26):9384–9389, 2014.

[21] Samuel IA Cohen, Sara Linse, Leila M Luheshi, Erik Hellstrand, Duncan A White, Luke Rajah, Daniel E Otzen, Michele Vendruscolo, Christopher M Dobson, and Tuomas PJ Knowles. Proliferation of amyloid-β42 aggregates occurs through a secondary nucleation mechanism. *Proceedings of the National Academy of Sciences*, 110(24):9758–9763, 2013.

[22] Paolo Arosio, Tuomas PJ Knowles, and Sara Linse. On the lag phase in amyloid fibril formation. *Physical Chemistry Chemical Physics*, 17(12):7606–7618, 2015.

[23] Erik Hellstrand, Barry Boland, Dominic M Walsh, and Sara Linse. Amyloid β-protein aggregation produces highly reproducible kinetic data and occurs by a two-phase process. *ACS chemical neuroscience*, 1(1):13–18, 2010.

[24] Veronica Lattanzi, Katja Bernfur, Emma Sparr, Ulf Olsson, and Sara Linse. Solubility of aβ40 peptide. *JCIS Open*, 4:100024, 2021.

[25] Thomas CT Michaels, Andela Šarić, Samo Curk, Katja Bernfur, Paolo Arosio, Georg Meisl, Alexander J Dear, Samuel IA Cohen, Christopher M Dobson, Michele Vendruscolo, et al. Dynamics of oligomer populations formed during the aggregation of alzheimer's aβ42 peptide. *Nature chemistry*, 12(5):445–451, 2020.

[26] Tinna Pálmadóttir, Christopher A Waudby, Katja Bernfur, John Christodoulou, Sara Linse, and Anders Malmendal. Morphology-dependent interactions between α-synuclein monomers and fibrils. *International journal of molecular sciences*, 24(6):5191, 2023.

[27] Alexander K Buell. Stability matters, too–the thermodynamics of amyloid fibril formation. *Chemical Science*, 13(35):10177–10192, 2022.

[28] Kai Gu, Xuefeng Liu, Yang Zhang, Hanwen Zhao, and Weiping Liu. Application of vacuum photoelectric detection technology in super-resolution system. *Optics and Photonics Journal*, 10(6):141–148, 2020.

[29] Claudette M St. Croix, Stuart H Shand, and Simon C Watkins. Confocal microscopy: comparisons, applications, and problems. *Biotechniques*, 39(sup6):S2–S5, 2005.

[30] James Jonkman and Claire M Brown. Any way you slice it—a comparison of confocal microscopy techniques. *Journal of biomolecular techniques: JBT*, 26(2):54, 2015.

[31] Samuel T Hess, Shaohui Huang, Ahmed A Heikal, and Watt W Webb. Biological and chemical applications of fluorescence correlation spectroscopy: a review. *Biochemistry*, 41(3):697–705, 2002.

[32] Stefan Wennmalm and Jerker Widengren. Inverse-fluorescence correlation spectroscopy: more information and less labeling. *Frontiers in Bioscience*, 3:385–392, 2011.

[33] Lan Yu, Yunze Lei, Ying Ma, Min Liu, Juanjuan Zheng, Dan Dan, and Peng Gao. A comprehensive review of fluorescence correlation spectroscopy. *Frontiers in physics*, 9:644450, 2021.

[34] Radek Macháň and Martin Hof. Fluorescence correlation spectroscopy (fcs). In *Practical Manual for Fluorescence Microscopy Techniques*, page 24. PicoQuant GmbH, 2016.

[35] Jan W Krieger, Anand P Singh, Nirmalya Bag, Christoph S Garbe, Timothy E Saunders, Jörg Langowski, and Thorsten Wohland. Imaging fluorescence (cross-) correlation spectroscopy in live cells and organisms. *Nature protocols*, 10(12):1948–1974, 2015.

[36] Stefan Wennmalm, Volodymyr Chmyrov, Jerker Widengren, and Lars Tjernberg. Highly sensitive fret-fcs detects amyloid β-peptide oligomers in solution at physiological concentrations. *Analytical chemistry*, 87(23):11700–11705, 2015.

[37] Sascha Schmitt, Lutz Nuhn, Matthias Barz, Hans-Jürgen Butt, and Kaloian Koynov. Shining light on polymeric drug nanocarriers with fluorescence correlation spectroscopy. *Macromolecular Rapid Communications*, 43(12):2100892, 2022.

[38] Stefan Wennmalm and Jerker Widengren. Interferometry and fluorescence detection for simultaneous analysis of labeled and unlabeled nanoparticles in solution. *Journal of the American Chemical Society*, 134(48):19516–19519, 2012.

[39] Georg Krainer, Raphael PB Jacquat, Matthias M Schneider, Timothy J Welsh, Jieyuan Fan, Quentin AE Peter, Ewa A Andrzejewska, Greta Šneiderienė, Magdalena A Czekalska, Hannes Ausserwoeger, et al. Single-molecule digital sizing of proteins in solution. *Nature Communications*, 15(1):7740, 2024.

[40] Thomas Müller, Paolo Arosio, Luke Rajah, Samuel IA Cohen, Emma V Yates, Michele Vendruscolo, Chrisopher M Dobson, and Tuomas PJ Knowles. Particle-based simulations of steady-state mass transport at high p\'eclet numbers. *arXiv preprint arXiv:1510.05126*, 2015.

[41] Sisi Zhou and Liang Jiang. Modern description of rayleigh's criterion. *Physical Review A*, 99(1):013808, 2019.

[42] Christian A Combs and Hari Shroff. Fluorescence microscopy: a concise guide to current imaging methods. *Current protocols in neuroscience*, 79(1):2–1, 2017.

[43] TS Baker, NH Olson, and SD Fuller. Adding the third dimension to virus life cycles: three-dimensional reconstruction of icosahedral viruses from cryo-electron micrographs. *Microbiology and Molecular Biology Reviews*, 63(4):862–922, 1999.

[44] Roman I Koning, Hildo Vader, Martijn van Nugteren, Peter A Grocutt, Wen Yang, Ludovic LR Renault, Abraham J Koster, Arnold CF Kamp, and Michael Schwertner. Automated vitrification of cryo-em samples with controllable sample thickness using suction and real-time optical inspection. *Nature Communications*, 13(1):2985, 2022.

[45] Roger S Macomber. *A complete introduction to modern NMR spectroscopy*. John Wiley & Sons, 1997.

[46] Alberto Tampieri, Márk Szabó, Francesc Medina, and Henrik Gulyás. A brief introduction to the basics of nmr spectroscopy and selected examples of its applications to materials characterization. *Physical Sciences Reviews*, 6(1):20190086, 2021.

[47] Amy M Ruschak and Andrew D Miranker. Fiber-dependent amyloid formation as catalysis of an existing reaction pathway. *Proceedings of the National Academy of Sciences*, 104(30):12341–12346, 2007.

[48] Alexander K Buell, Céline Galvagnion, Ricardo Gaspar, Emma Sparr, Michele Vendruscolo, Tuomas PJ Knowles, Sara Linse, and Christopher M

Dobson. Solution conditions determine the relative importance of nucleation and growth processes in α-synuclein aggregation. *Proceedings of the National Academy of Sciences*, 111(21):7671–7676, 2014.

[49] Diana C Rodriguez Camargo, Sean Chia, Joseph Menzies, Benedetta Mannini, Georg Meisl, Martin Lundqvist, Christin Pohl, Katja Bernfur, Veronica Lattanzi, Johnny Habchi, et al. Surface-catalyzed secondary nucleation dominates the generation of toxic iapp aggregates. *Frontiers in Molecular Biosciences*, 8:757425, 2021.

[50] Thomas C. T. Michaels, Andela Šarić, Samo Curk, Katja Bernfur, Paolo Arosio, Georg Meisl, Alexander J. Dear, Samuel I. A. Cohen, Christopher M. Dobson, Michele Vendruscolo, Sara Linse, and Tuomas P. J. Knowles. Dynamics of oligomer populations formed during the aggregation of alzheimer's aβ42 peptide. *Nat. Chem.*, 12(5):445–451, May 2020.

[51] Catherine K. Xu, Georg Meisl, Ewa A. Andrzejewska, Georg Krainer, Alexander J. Dear, Marta Castellana-Cruz, Soma Turi, Irina A. Edu, Giorgio Vivacqua, Raphaël P. B. Jacquat, William E. Arter, Maria Grazia Spillantini, Michele Vendruscolo, Sara Linse, and Tuomas P. J. Knowles. α-synuclein oligomers form by secondary nucleation. *Nat. Commun.*, 15(1):7083, Aug 2024.

[52] Ricardo Gaspar, Georg Meisl, Alexander K Buell, Laurence Young, Clemens F Kaminski, Tuomas PJ Knowles, Emma Sparr, and Sara Linse. Secondary nucleation of monomers on fibril surface dominates α-synuclein aggregation and provides autocatalytic amyloid amplification. *Quarterly reviews of biophysics*, 50:e6, 2017.

[53] Georg Meisl, Catherine K Xu, Jonathan D Taylor, Thomas C T Michaels, Aviad Levin, Daniel Otzen, David Klenerman, Steve Matthews, Sara Linse, Maria Andreasen, and Tuomas P. J. Knowles. Uncovering the universality of self-replication in protein aggregation and its link to disease. *Sci. Adv.*, from review:eabn6831, 2022.

[54] Alexander J Dear, Georg Meisl, Thomas CT Michaels, Manuela R Zimmermann, Sara Linse, and Tuomas PJ Knowles. The catalytic nature of protein aggregation. *The Journal of Chemical Physics*, 152(4), 2020.

[55] Samuel IA Cohen, Sara Linse, Leila M Luheshi, Erik Hellstrand, Duncan A White, Luke Rajah, Daniel E Otzen, Michele Vendruscolo, Christopher M Dobson, and Tuomas PJ Knowles. Proliferation of amyloid-β42 aggregates occurs through a secondary nucleation mechanism. *Proceedings of the National Academy of Sciences*, 110(24):9758–9763, 2013.

[56] Ursula Florjanczyk, Derek P Ng, Stavroula Andreopoulos, and Jodie Jenkinson. Developing a three-dimensional animation for deeper molecular understanding of michaelis–menten enzyme kinetics. *Biochemistry and Molecular Biology Education*, 46(5):561–565, 2018.

[57] Georg Meisl, Xiaoting Yang, Erik Hellstrand, Birgitta Frohm, Julius B. Kirkegaard, Samuel I. A. Cohen, Christopher M. Dobson, Sara Linse, and Tuomas P. J. Knowles. Differences in nucleation behavior underlie the contrasting aggregation kinetics of the Aβ40 and Aβ42 peptides. *Proceedings of the National Academy of Sciences*, 111(26):9384–9389, July 2014. Publisher: National Academy of Sciences Section: Physical Sciences.

[58] Samuel IA Cohen, Paolo Arosio, Jenny Presto, Firoz Roshan Kurudenkandy, Henrik Biverstål, Lisa Dolfe, Christopher Dunning, Xiaoting Yang, Birgitta Frohm, Michele Vendruscolo, et al. A molecular chaperone breaks the catalytic cycle that generates toxic aβ oligomers. *Nature structural & molecular biology*, 22(3):207–213, 2015.

[59] Su-Mi Hur, Vikram Thapar, Abelardo Ramírez-Hernández, Gurdaman Khaira, Tamar Segal-Peretz, Paulina A Rincon-Delgadillo, Weihua Li, Marcus Müller, Paul F Nealey, and Juan J de Pablo. Molecular pathways for defect annihilation in directed self-assembly. *Proceedings of the National Academy of Sciences*, 112(46):14144–14149, 2015.

[60] Alana Pauls, Ally Dunnum, Andrew Martin, Ava Huth, Chuanshen Du, and Martin Thuo. Correcting edge defects in self-assembled monolayers through thermal annealing. *ChemPhysChem*, page e202400626, 2024.

[61] Donald Edward Hicks. Thermophysical properties of the amyloid beta protein from differential scanning calorimetry. 2005.

[62] Mathew Sebastiao, Noe Quittot, and Steve Bourgault. Thioflavin t fluorescence to analyse amyloid formation kinetics: Measurement frequency as a factor explaining irreproducibility. *Analytical biochemistry*, 532:83–86, 2017.

[63] Mattias Törnquist, Risto Cukalevski, Ulrich Weininger, Georg Meisl, Tuomas PJ Knowles, Thom Leiding, Anders Malmendal, Mikael Akke, and Sara Linse. Ultrastructural evidence for self-replication of alzheimer-associated aβ42 amyloid along the sides of fibrils. *Proceedings of the National Academy of Sciences*, 117(21):11265–11273, 2020.

[64] Katarzyna Makasewicz, Stefan Wennmalm, Bjorn Stenqvist, Marco Fornasier, Alexandra Andersson, Peter Jonsson, Sara Linse, and Emma Sparr.

Cooperativity of α-synuclein binding to lipid membranes. *ACS Chemical Neuroscience*, 12(12):2099–2109, 2021.

[65] Jefferson D Knight, James A Hebda, and Andrew D Miranker. Conserved and cooperative assembly of membrane-bound α-helical states of islet amyloid polypeptide. *Biochemistry*, 45(31):9496–9508, 2006.

[66] Sara Linse, Kyrre Thalberg, and Tuomas PJ Knowles. The unhappy chaperone. *QRB discovery*, 2:e7, 2021.

[67] Andreas Carlsson, Emil Axell, Cecilia Emanuelsson, Ulf Olsson, and Sara Linse. The ability of dnajb6b to suppress amyloid formation depends on the chaperone aggregation state. *ACS Chemical Neuroscience*, 15(9):1732–1737, 2024.

[68] Jing Hu, Sara Linse, and Emma Sparr. Ganglioside micelles affect amyloid β aggregation by coassembly. *ACS Chemical Neuroscience*, 14(24):4335–4343, 2023.